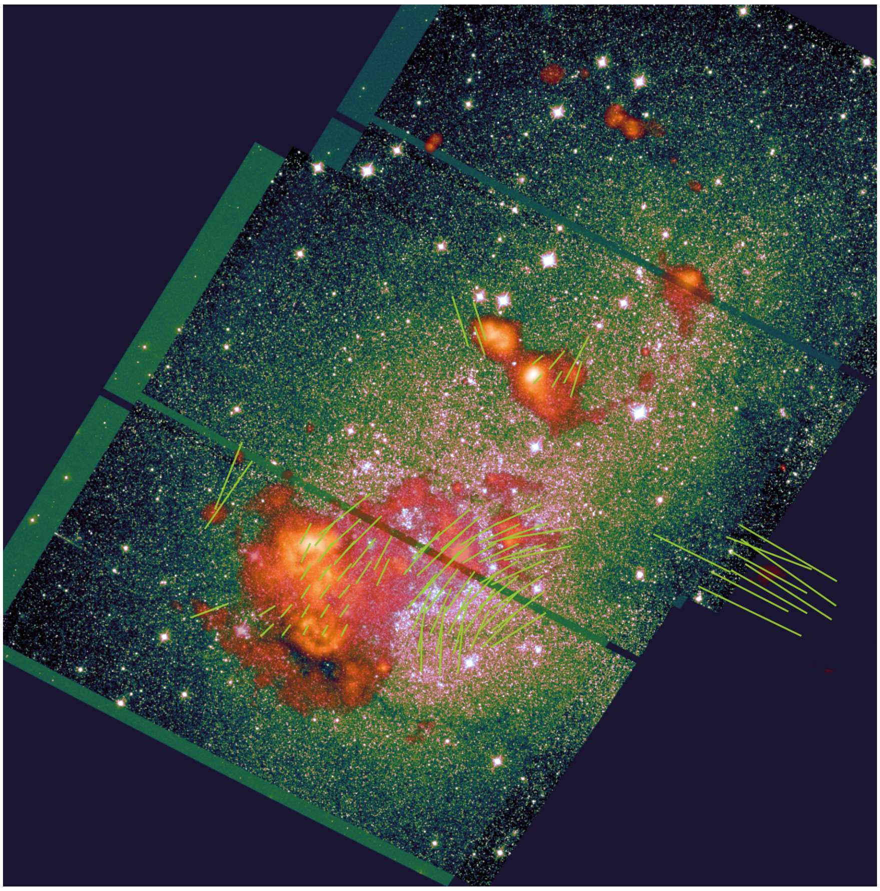

Exploring polarisation and dust grain alignment in a dwarf galaxy

Thesis for the degree of Master of Science in Physics

MAJA RHODIN

DEPARTMENT OF PHYSICS AND ASTRONOMY
CHALMERS UNIVERSITY OF TECHNOLOGY
Gothenburg, Sweden 2026
www.chalmers.se

Master's thesis 2026

Exploring polarisation and dust grain alignment in a dwarf galaxy

MAJA RHODIN

CHALMERS
UNIVERSITY OF TECHNOLOGY

Department of Physics and Astronomy
Division of Astronomy and Plasma Physics
Gina Panopoulou's research group
Chalmers University of Technology
Gothenburg, Sweden 2026

Exploring polarisation and dust grain alignment in a dwarf galaxy
MAJA RHODIN

© MAJA RHODIN, 2026.

Examiner and supervisor: Asst Prof. Georgia V. Panopoulou, Department of Physics and Astronomy

Master's Thesis 2026
Department of Physics and Astronomy
Division of Astronomy and Plasma Physics
Gina Panopoulou's research group
Chalmers University of Technology
SE-412 96 Gothenburg
Telephone +46 31 772 1000

Front cover: Different views of the dwarf galaxy IC 10; its stellar component, central regions of Hα emission and magnetic-field lines.

Back cover: My dog Saga last summer in the kitchen sofa.

Typeset in LaTeX
Printed by Chalmers Reproservice
Gothenburg, Sweden 2026

Exploring magnetic fields and dust grain alignment in a dwarf galaxy
MAJA RHODIN
Department of Physics and Astronomy
Chalmers University of Technology

Abstract

The nature and origin of magnetic fields in galaxies remain key questions in galactic evolution. Much of our knowledge of these fields relies on observations of polarised light in Milky-Way-type galaxies. In such systems, the interstellar radiation field, magnetic field, and gas interact with dust grains causing the grains to align with the magnetic field. This alignment gives rise to polarised dust emission, allowing the magnetic field orientation to be mapped. However, theoretical calculations indicate that alignment depends sensitively on the underlying properties of the interstellar medium (ISM). This work investigates dust grain alignment in a system with different characteristics from typical Milky Way type galaxies: the dwarf galaxy IC 10.
The dust temperatures for IC 10 is derived by fitting modified blackbody (MBB) models to data from the *Herschel* Spectral and Photometric Imaging Receiver (SPIRE). Neutral atomic hydrogen (H I) column densities produced from the Very Large Array (VLA) are used as an estimate of the gas column densities in the galaxy, and other relevant ISM properties such as magnetic field strengths were collected from the literature to enter the radiative alignment torque (RAT) calculations. Timescales for dust grain alignment with the magnetic and radiation fields respectively (B-RAT and k-RAT) are calculated, along with the timescale of gas damping effects on the dust grains. Timescales of these processes are calculated for different grain sizes. Additional constraints are calculated with a numerical iteration method on the grain size range that permits alignment by implementing the criterions on dust suprathermal rotation and radiative torque disruption (RAT-D).
RAT induced dust grain alignment is found to be possible under the ISM conditions of IC 10 and that B-RAT dominates throughout the investigated regions. Grain alignment in IC 10 operates similarly to how it does in the Milky Way-like galaxy M51. The radiation field plays a key role in determining the radiative torque efficiency ($\boldsymbol{Q}_\Gamma$) and in regulating grain disruption. The absence of reliably detected polarised emission in parts of the galaxy does not therefore necessarily imply the absence of aligned dust grains in those regions. Our calculations predict significant variations in the sizes of aligned grains across IC10, which can be tested by optical polarimetry in the future.

Keywords: polarisation, interstellar medium, dwarf galaxies, dust, magnetic fields

Acknowledgements

First and foremost, I would like to express my greatest thanks to my supervisor, Gina Panopoulou, for her endless support and enthusiasm throughout this project. Thank you for introducing me to this fascinating subject in the broad field that is interstellar astronomy which I might never have found on my own, and for giving me the opportunity to immerse myself in it through this project. Over these past months I have learned so much not only about this unique and exciting area of astronomy, but about the research process itself. Your guidance and belief in my work has been invaluable.

I would also like to thank the members of Gina Panopoulou's research group for making me feel very welcomed, and a special thanks to Siddharth Kumar for our chats and for his help in figuring out the RAT mechanism.

My sincere thanks to Enrique Lopez-Rodriguez, whose work this study was based upon. Your enthusiastic and encouraging response when I presented my results to you and your student Reagan this spring meant a great deal.

Lastly, I would like to thank my friends for all their support, and especially my family for their constant encouragement and the curiosity and interest they have shown in my work.

Maja Rhodin, Gothenburg, June 2026

List of Acronyms

The acronyms used throughout this thesis are listed below in alphabetical order.

B-RAT	Magnetic-field alignment through radiative torques
CO	Carbon monoxide
DDA	Discrete dipole approximation
FIR	Far-infrared
FWHM	Full width at half maximum
GNILC	Generalized Needlet Internal Linear Combination
HAWC+	High-resolution Airborne Wideband Camera Plus
H I	Neutral atomic hydrogen
H II	Ionised hydrogen
IR	Infrared
ISRF	Interstellar radiation field
ISM	Interstellar medium
k-RAT	Radiation-field alignment through radiative torques
LMC	Large Magellanic Cloud
MBB	Modified blackbody
PACS	Photodetector Array Camera and Spectrometer
RAT	Radiative alignment torque
RAT-D	Radiative torque disruption
SALSA	Survey on extragALactic magnetiSm with SOFIA
SED	Spectral energy distribution
SOFIA	Stratospheric Observatory for Infrared Astronomy
SPIRE	Spectral and Photometric Imaging Receiver
VLA	Karl G. Jansky Very Large Array

Nomenclature

Radiation and polarisation

I, Q, U, V	Stokes parameters
P	Polarised flux
p	Polarisation fraction or effective magnetic moment factor, as specified in context
$I_{\rm min}, I_{\rm max}$	Minimum and maximum measured intensities
ψ	Polarisation angle; also the angle between the magnetic and radiation fields where specified
χ	Ellipticity angle
u_λ	Spectral radiation energy density
$u_{\rm rad}$	Total radiation energy density
$u_{\rm ISRF}$	Energy density of the local interstellar radiation field
$\lambda, \bar{\lambda}$	Radiation wavelength and energy-weighted mean wavelength
ν, ν_0	Frequency and reference frequency
γ	Radiation-field anisotropy factor
Q_{e3}	Radiative-torque efficiency component responsible for precession
$\mathbf{Q}_{\mathbf{\Gamma}}$	Dimensionless radiative-torque efficiency vector

Dust grain properties

a	Grain size, identified with the semimajor axis
a_1, a_2, a_3	Grain semiaxes
$a_{\rm eff}$	Effective grain size
$a_{\rm min}, a_{\rm max}$	Minimum and maximum grain sizes
$a_{\rm align}$	Minimum grain size for efficient alignment
$a_{\rm disr}$	Characteristic grain size for rotational disruption
s	Grain axial ratio
V	Grain volume

$\rho, \rho_{\rm sil}$	Grain mass density and silicate-grain mass density
$I_1, I_{\parallel}$	Principal moment of inertia about the grain symmetry axis
$n_{\rm sil}$	Number density of atoms in the silicate material
f_p	Fraction of paramagnetic atoms in the grain material
$S_{\rm max}$	Maximum tensile strength of a grain
$\chi(0)$	Static magnetic susceptibility

Dynamics and environmental quantities

$\boldsymbol{J}$	Grain angular momentum
$\boldsymbol{\Gamma}$	Torque
$\boldsymbol{\Gamma}_{\rm RAT}$	Radiative torque
ω	Angular velocity
$\omega_{\rm th}$	Thermal angular velocity
$\omega_{\rm RAT}$	Angular velocity induced by radiative torques
$\omega_{\rm disr}$	Critical angular velocity for rotational disruption
$\tau_{\rm Lar}$	Larmor precession timescale
$\tau_{\rm k\text{-}RAT}$	Radiative-precession timescale
$\tau_{\rm gas}$	Gas-damping timescale
$\tau_{\rm damp}$	Total rotational-damping timescale
$F_{\rm IR}$	Infrared rotational-damping factor
B	Magnetic-field strength
T_d, T_g	Dust and gas temperatures
$n_{\rm H}$	Hydrogen volume density
$N_{\rm H}$	Hydrogen column density
m_H	Hydrogen-atom mass
μ	Mean gas mass per hydrogen atom

Modified blackbody fitting

$\mathcal{B}_\nu$	Planck function
β	Dust emissivity spectral index
τ_{ν_0}	Dust optical depth at reference frequency ν_0
κ_{ν_0}	Dust mass absorption coefficient at reference frequency ν_0
Σ_d, Σ_g	Dust and gas surface mass densities
$R_{\rm gd}$	Gas-to-dust mass ratio

K_{ColE}	Extended-source Colour correction factor

Contents

List of Figures

List of Tables

1

Introduction

1.1 Magnetic fields and dust-grain alignment

Magnetic fields are one of the fundamental components of the interstellar medium (ISM) [4]. They influence the motion of charged particles, affect the transport of cosmic rays, and may play an important role in regulating processes such as star formation and the evolution of galaxies [5]. Despite their importance, magnetic fields cannot be observed directly. Instead, their presence and structure must be inferred through their interaction with other components of the ISM.

One of the most powerful methods for tracing magnetic fields relies on the polarisation of interstellar light. In the infrared (IR) and submillimetre regimes, polarisation arises because interstellar dust grains of generally asymmetric shapes will tend to align like a lattice with respect to the local magnetic field. As a result, the thermal emission from the grains becomes polarised, allowing the orientation of the magnetic field projected on the plane of the sky to be inferred from polarisation observations. Furthermore, the optical light from stars will be filtered through this aligned dust producing polarised light that traces the magnetic field.

The connection between polarisation and interstellar dust was established shortly after the first detections of polarised starlight in 1949 [6, 7]. It was quickly proposed that elongated dust grains aligned with the galactic magnetic field could explain the observed polarisation signal. This idea set the stage for decades of theoretical and observational research to understand how this alignment works, and what are the driving mechanisms.

Since then, many ideas as to the exact alignment mechanism have been proposed, revisited and tested. As observational evidence accumulated, and laboratory experiments and simulations improved, many of the early candidates were proved unable to explain the full range of observed properties (see Table 1 of the Andersson review 2015 [8]). Today, the most widely supported explanation is the theory of Radiative Alignment Torques (RATs). It is believed to be the primary aligning mechanism in a majority of settings. In this framework, anisotropic radiation interacts with irregularly shaped dust grains, exerting torques that spin up the grains to suprathermal rotation velocities. The process can be compared to the wind acting on a windmill, where the asymmetric grain shape allows for incident radiation to transfer angular momentum to the grain, just like the wind transfers angular momentum to the windmill's rotor blades. Once the grains rotate at sufficient speeds, they are not as easily perturbed by their surroundings and can instead become aligned with respect to the local magnetic field.

Historically, grain alignment has been studied up to great detail in the Milky Way and other Milky Way-type galaxies (see the review by Andersson et al., 2015 [8]). Even though RAT theory has been highly successful in explaining many observations, it predicts that the dust grain alignment to magnetic field has a delicate dependence on the underlying conditions of the ISM. As a result, the efficiency of grain alignment can vary significantly between different astrophysical environments [9].

Atypical ISM environments are thus an ideal laboratory for testing the effectiveness of RAT alignment. So far, the most 'extreme' interstellar environment where RATs have been tested is a star-forming region in the LMC (Tram et al. [10]). In this work, we wish to explore whether and how grain alignment can occur over different regions in a galaxy that is very different from the Milky Way.

1.2 Research subject: the dwarf galaxy IC 10

The subject of this study is the dwarf galaxy IC 10, located in the constellation Cassiopeia at a distance of approximately 0.7 Mpc from the Sun [11]. It is the nearest starburst galaxy in the Local Group [12]. Its apparent angular size is $6.8' \times 5.9'$, corresponding to an optical diameter of approximately 3.81 kpc [13]. In addition to its stellar body, IC 10 is embedded in an wide envelope of neutral hydrogen gas, spanning roughly $68' \times 80'$ on the sky [14]. Morphologically, IC 10 is classified as an irregular dwarf galaxy and it is characterised by a relatively high star formation rate, estimated to be ~ 0.04–$0.08\,\mathrm{M_\odot\,yr^{-1}}$ [14]. Observations of Hα reveal strong emission regions throughout the galaxy, particularly in the south eastern (astronomical left) region highlighted in Figure 1.1. Since Hα emission traces recombination in ionised hydrogen that has recently been produced by young, massive stars, it is consistent with the classification of IC 10 as a starburst galaxy [15]. Furthermore, IC 10 has a relatively low metallicity, approximately $Z \approx 0.2\,Z_\odot$ [15], implying a lower abundance of heavy elements and dust grains compared to the Milky Way.

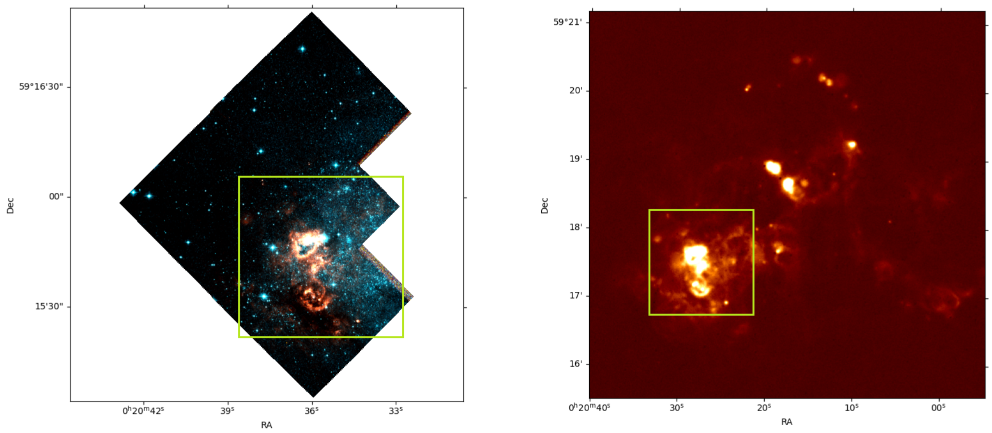

Figure 1.1: Different views of IC 10. To the left, zoomed-in view showing the stellar component of IC 10 (blue colours) and the Hα emission over the central star-forming region (red) (source: Hubble Space Telescope). To the right, ionized gas traced by Hα emission in the optical (source: Palomar telescope). The green squares mark the south eastern region of strong Hα emission.

This irregular morphology and its stellar mass of $6.7 - 8.1 \times 10^8\, M_\odot$ [16], which is relative to the larger Milky Way type galaxies, creates a setting that differs a lot from the ones typically investigated in grain alignment studies. Furthermore, IC 10 has been studied extensively across a wide range of wavelengths, from the radio to the optical. As a result, many of its large scale properties, including magnetic field strengths, gas densities, and star formation characteristics, are well known [17]. IC 10 therefore provides a unique setting for investigating ISM conditions that differ substantially from those of typical Milky-Way-type galaxies.

1.3 Report structure

This thesis is organised as follows. Chapter 2 introduces the theoretical framework underlying dust grain alignment, polarisation, radiative torques, and grain disruption. Chapter 3 first presents the full observation of polarised light from the Stratospheric Observatory for Infrared Astronomy (SOFIA) and the extraction of reliable polarisation data from the observation. It then describes the full derivation of the dust temperature and gas column density maps from Herschel observations. Finally, it presents the observational data and environmental parameters adopted for M51 and IC 10, along with the numerical methods used to calculate alignment and disruption timescales, angular velocities, and characteristic grain size limits. The resulting dust temperature map, the timescale calculations and grain size constraints are presented in Chapter 4. Chapter 5 discusses the implications of the results in the context of grain alignment theory and the polarisation observations. Finally, Chapter 6 summarises the main conclusions of this work and outlines possible directions for future investigations.

2
Theory

This chapter presents the necessary theoretical background for this thesis. An introduction to astronomical polarimetry along with relevant parameters are first presented in Section 2.1. Section 2.2 then describes interstellar dust grains and their roll in the interstellar medium (ISM). In Section 2.3, the theory of Radiative Alignment Torques (RATs) is presented.

2.1 Polarimetry

Polarised light is observed in many galaxies, and commonly follows macroscopic patterns over the galaxies. The polarised light is formed when stellar radiation is reddened by the ISM, and some parts, namely the asymmetric dust particles, absorb and re-emit the stellar light more along one of its sides than the other. When the grains have one side that is tangibly larger than the other in its orientation perpendicular to the stellar radiation, the longer side can absorb more light than its shorter side. The reemitted light will then also have greater intensity from the grains long side and less intensity from its short side [1].
The light is then partially plane polarised and can be measured with an astronomical polarimeter. This device measures the linear intensity of the light at different angles and finds a maximum and minimum intensity, $I_{\max}$ and $I_{\min}$, at two orthogonal angles. The degree of polarisation of the radiation is defined as

$$p = \frac{I_{\max} - I_{\min}}{I_{\max} + I_{\min}}. \tag{2.1}$$

To fully describe the characteristics of the polarised light, namely its ellipticity and orientation in the sky, the measured data can be expressed in a set of parameters called the Stokes parameters I, Q, U and V. For plane polarised light, which is the most common form of interstellar polarisation, the Stokes parameters are given by

$$\begin{aligned} I &= I_{\max} + I_{\min}, \\ Q &= pI\cos(2\psi)\cos(2\chi), \\ U &= pI\sin(2\psi)\cos(2\chi), \\ V &= pI\sin(2\chi), \end{aligned} \tag{2.2}$$

where ψ is the polarisation angle and χ is the ellipticity angle (see Figure 2.1 (right)) [1]. A visual representation of the orientations of polarising filters that go into the measurement of each Stokes parameter is shown in Figure 2.1 (left).

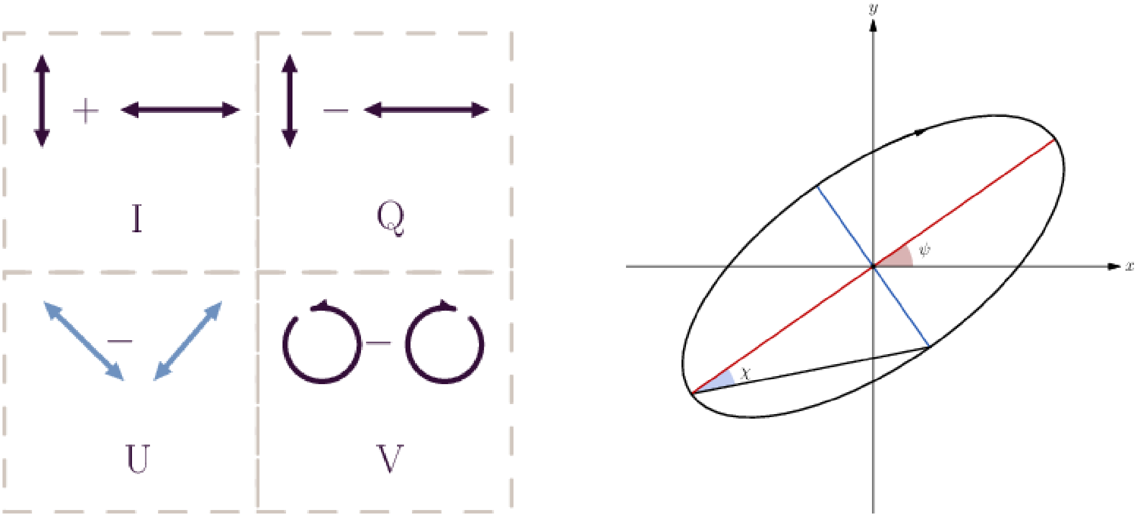

Figure 2.1: Stokes parameters as they are calculated from six polarisation filters to the left, and the definition of the polarisation angle ψ and the ellipticity angle χ to the right.

It is with these parameters that polarised radiation can be traced over entire galaxies, and by extension the patterns they form. A common way of presenting the polarisation in a galaxy is to draw the linear polarisation vectors at each point. The polarisation vectors length and orientation are determined by the degree of polarisation (determined by χ) and by ψ. An example of linear polarisation distribution in the Milky Way is presented in Figure 2.2.

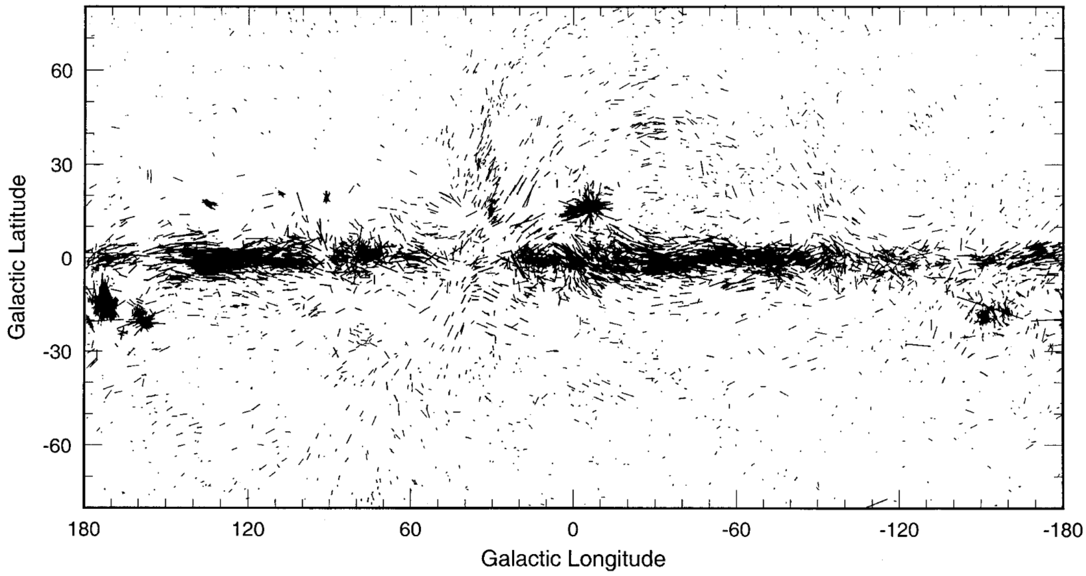

Figure 2.2: Distribution of linear polarisation vectors in galactic coordinates in the Milky Way. The length and orientation of each vector represents the polarisation degree and position angle for a star at that location. This figure is taken from Whittet (2003) [1].

In this Figure, we can see large patterns stretching across the whole galaxy as well as smaller, more locally dominating patterns and chaos. The large-scale ordered pattern seen along the plane of the Galaxy, traces the ordered component of the magnetic field which we now know is parallel to the disk of the Galaxy. Smaller-scale random patterns are seen typically around star-forming regions, where gravity, turbulence, and stellar feedback shape the magnetic field lines. The complexity of the ISM conditions can already be deduced by these stark variations. In the next subchapters, we discuss how the ISM components such as the radiation and magnetic fields interact with the gas and dust grains to produce the phenomenon of grain alignment and hence the observed polarisation.

2.2 Grain model and properties

We know that the grains align systematically, with their shortest axis, that is their axis of largest moment of inertia, along the field lines of the galactic magnetic field. This gives us clues on the dust grains' composition letting it interact with the magnetic field, their physical structure and size. It also reveals what environmental conditions they are exposed to, and of their consequent dynamics that allows for the alignment to happen.

The materials that are believed to make up the dust in the ISM consist of elements that are not very common in the gas phase. Assuming that the ISM has a closely similar composition to that observed in the solar photosphere, the primary dust grain building blocks that are locked away in interstellar dust are C, O, Mg, Si, S and Fe [18]. These elements form many different materials that can generally be catalogued in two groups of materials: silicates and carbons [18] [19]. The exact composition of these elements is an entire field of research in itself. In studies of grain alignment, the assumed overall composition of the grains is most commonly that of $MgFeSiO_4$. This is a crystalline material in the olivine structural family. Due to its inclusion of Fe, the material is paramagnetic and can interact with external magnetic fields.

It is common to model the dust grains as having an entirely oblate spheroidal shape, $a_1 < a_2 = a_3$, where a_1 is the size along the semi-minor axis $\hat{a}_1$ and a_2 is the size along their semi-major axis $\hat{a}_2$ and $\hat{a}_2 \perp \hat{a}_3$, see Figure 2.3. The ratio of its sides have a best-fit of $s = a_1/a_2 = 2/3$ (e.g. Draine & Hensley [20]). Because a_2 describes the broad side of the grains, it is referred to as the grain size $a \equiv a_2$.

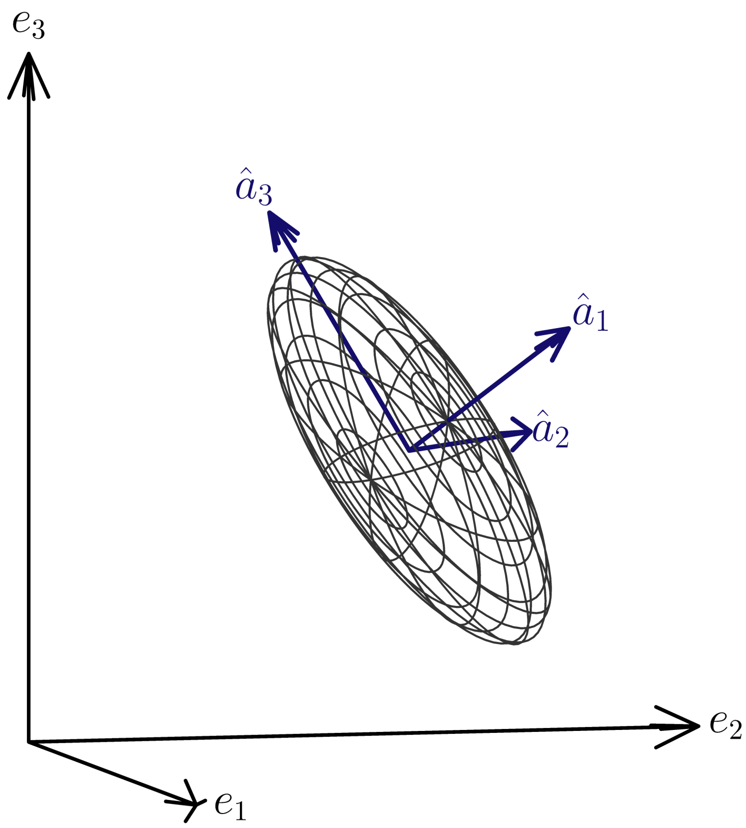

Figure 2.3: Definition of the grain body coordinate system ($\hat{a}_1$, $\hat{a}_2$, $\hat{a}_3$) in an arbitrary Cartesian coordinate system ($\hat{e}_1$, $\hat{e}_2$, $\hat{e}_3$). $\hat{a}_1$ correspond to the semi-minor axis, short axis, of the grain while $\hat{a}_2$ and $\hat{a}_3$ are the long axis of the oblate grain.

For models that include these types of silicates, the size distribution of the grains is a power law, $dn/da \propto a^{-3.5}$ within the range of possible grain sizes, $a_{\min} < a < a_{\max}$. The smallest grains have a minimum size of around $a_{\min} \simeq 0.005\,\mu\text{m}$, and the largest grains reach a size up to $a_{\max} \simeq 0.02\,\mu\text{m}$ [21].

Because the dust grains in the ISM are systematically aligned to some external field, their kinetic energy will not be in equilibrium with the gas kinetic energy. Otherwise their rotational excitation would be dominated by random collisions with the gas. Due to its randomness, would be Brownian in nature and thus unable to give the grains a consistently big enough angular momentum that it can, stabilise the grains. The grains will tumble and be unable to align around any consistent axis. In order for the grains to obtain a stable and fixed angular momentum, they need to rotate at suprathermal rates at which $T_{dust} \gg T_{gas}$, so that it is not perturbed by thermal noise [18]. It turns out that grains achieve these rotation rates by transfer of angular momentum from stellar radiation to the grains as the field acts on them with a stable radiation torque. This torque will not only spin up the grains to the suprathermal speeds, but it will also if large enough cause the grains to change their direction.

2.3 RAT theory

The first part of this Section 2.3.1, presents a simplified derivation of the radiative torque based on the discrete dipole approximation. The full external grain dynamics are then put in the perspective of external torques with the equation of motion in Section 2.3.2, after which the external torques are explained one by one in Section 2.3.3. Finally, the minimum size limit for grains to be aligned, and the upper size limit not to be disrupted by the spin-induced internal stress, are presented based on rotation criteria in Section 2.3.4.

2.3.1 Radiative torque derivation with the discrete dipole approximation

General reference to this section: the article Radiative Torques on Interstellar Grains: I. Superthermal Spinup, by B. T. Draine (1997).

We wish to describe the radiation fields and their effect on polarisable components in grains in general terms and adapt the discrete dipole approximation (DDA). In this framework, we approximate the target grain to be a grid of polarisable points, placed at $\boldsymbol{r}_j$ and with electric polarisability α_j, and letting the space between the points be vacuum.
We let the grain be hit with monochromatic light of wavelength ω_0 and with propagation vector $\boldsymbol{k} = k\hat{\boldsymbol{k}}$ where $k = \omega_0/c$. The incident electromagnetic field on each lattice point j will be

$$\boldsymbol{E}_{\mathbf{inc},j} = \boldsymbol{E}_{\mathbf{inc},0}\, e^{i(\boldsymbol{k}\cdot\boldsymbol{r}_j - \omega_0 t)} \tag{2.3}$$

$$\boldsymbol{B}_{\mathbf{inc},j} = \boldsymbol{B}_{\mathbf{inc},0}\, e^{i(\boldsymbol{k}\cdot\boldsymbol{r}_j - \omega_0 t)} \tag{2.4}$$

$$\boldsymbol{B}_{\mathbf{inc},0} = \hat{\boldsymbol{k}} \times \boldsymbol{E}_{\mathbf{inc},0}. \tag{2.5}$$

All points will become polarised from the imposing electric field and each gain a dipole moment

$$\boldsymbol{p}_j = \alpha_j\, \boldsymbol{E}_j. \tag{2.6}$$

Each point will then also be affected by a scattering field created by all its neighbouring points we call l, $\boldsymbol{E}_{\mathbf{sca},j} = \boldsymbol{E}(\boldsymbol{r}_{jl}, \boldsymbol{p}_l)_{l\neq j}$. Thus the total electromagnetic field on each point j will stem from the incident field and from all dipoles except for j,

$$\boldsymbol{E}_j = \boldsymbol{E}_{\mathbf{inc},j} + \boldsymbol{E}_{\mathbf{sca},j} \tag{2.7}$$

and likewise

$$\boldsymbol{B}_j = \boldsymbol{B}_{\mathbf{inc},j} + \boldsymbol{B}_{\mathbf{sca},j}. \tag{2.8}$$

The electromagnetic field will produce an instantaneous force on the point dipole j, $\boldsymbol{F}_j$. The total radiative force on the body, $\boldsymbol{F}_{\mathbf{rad}} = \sum_j \boldsymbol{F}_j$ can in a corresponding manner to the field be divided into components,

$$\boldsymbol{F}_{\mathbf{rad}} = \boldsymbol{F}_{\mathbf{inc}} + \boldsymbol{F}_{\mathbf{sca}}. \tag{2.9}$$

Taking time average of each component,

$$\langle \boldsymbol{F}_{\mathbf{rad}} \rangle = \langle \boldsymbol{F}_{\mathbf{inc}} \rangle + \langle \boldsymbol{F}_{\mathbf{sca}} \rangle, \tag{2.10}$$

we can show that the first component is equal to

$$\langle \boldsymbol{F}_{\mathbf{inc}} \rangle = \frac{1}{8\pi} C_{\mathbf{ext}} |\boldsymbol{E}_{\mathbf{inc},0}|^2 \hat{\boldsymbol{k}} \tag{2.11}$$

where $C_{\mathbf{ext}}$ is the total extinction correction on the grain, so that it describes the average rate at which the incident field loses its momentum. $\langle \boldsymbol{F}_{\mathbf{sca}} \rangle$ can be thought of simply as the recoil effect on the grain due to the scattered radiation. To simplify and generalise the radiation force, we can introduce a dimensionless radiation pressure efficiency vector we call $\boldsymbol{Q}_{\mathbf{pr}}$, so that the radiation pressure force can be rewritten

$$\langle \boldsymbol{F}_{\mathbf{rad}} \rangle = \boldsymbol{Q}_{\mathbf{pr}} \pi a_{\mathbf{eff}}^2 \frac{|\boldsymbol{E}_{\mathbf{inc},0}|^2}{8\pi}. \tag{2.12}$$

$\boldsymbol{Q}_{\mathbf{pr}}$ will then contain all the constraints from the grain orientation relative to the incident radiation direction that will determine the efficiency of the radiation pressure on the grain. What is enough for the intuition of this vector is that the quantity $\boldsymbol{Q}_{\mathbf{pr}} \cdot \hat{\boldsymbol{k}}$ will be equal to $Q_{\mathbf{pr}} \equiv C_{\mathbf{pr}}/\pi a_{\mathbf{eff}}^2$ where $C_{\mathbf{pr}}$ is the classical radiation pressure cross section

$$C_{\mathbf{pr}} = C_{\mathbf{abs}} + (1 + \langle \cos\theta \rangle) C_{\mathbf{sca}} \tag{2.13}$$

where $\langle \cos\theta \rangle$ is the mean value of $\cos\theta$ of scattered radiation for scattering angle θ. The radiation field will produce an instantaneous radiative torque on the grain that can be expressed

$$\boldsymbol{\Gamma}_{\mathbf{rad}} = \sum_{j=1}^{N} \boldsymbol{r}_j \times \boldsymbol{F}_j + \sum_{j=1}^{N} \mathrm{Re}(\boldsymbol{p}_j) \times \mathrm{Re}(\boldsymbol{E}_j). \tag{2.14}$$

Like the radiative force too can be divided into an incident and scattered component

$$\boldsymbol{\Gamma}_{\mathbf{rad}} = \boldsymbol{\Gamma}_{\mathbf{inc}} + \boldsymbol{\Gamma}_{\mathbf{sca}} \tag{2.15}$$

and similarly, the time averaged torque can be calculated and simplified with a corresponding torque efficiency vector $\mathbf{Q}_{\boldsymbol{\Gamma}}$,

$$\langle \boldsymbol{\Gamma}_{\mathbf{rad}} \rangle = \mathbf{Q}_{\boldsymbol{\Gamma}} \pi a_{\mathbf{eff}}^2 \frac{|\boldsymbol{E}_{\mathbf{inc},0}|^2}{8\pi k} = \pi a_{\mathbf{eff}}^2 u_\lambda \frac{\lambda}{2\pi} \mathbf{Q}_{\boldsymbol{\Gamma}}. \tag{2.16}$$

where $u_\lambda = |\boldsymbol{E}_{\mathbf{inc},0}|^2/8\pi$ is the time-averaged energy density of the incident radiation of wavelength λ.

Specifying this to the radiation from stars, we want to both average the relevant torque components over the entire wavelength spectrum, so called spectral averaging, and directly account for the anisotropy of the radiation field. We define

$$u_{rad} = \int u_\lambda d\lambda \tag{2.17}$$

as the total starlight energy density, and take the spectral average of the wavelengths and the torque efficiency factor

$$\bar{\lambda} = \frac{\int \lambda u_\lambda d\lambda}{u_{rad}}, \tag{2.18}$$

$$\langle \mathbf{Q_\Gamma} \rangle_\lambda = \frac{\int \mathbf{Q_\Gamma} \lambda u_\lambda d\lambda}{u_{rad}} \tag{2.19}$$

where $\langle\rangle_\lambda$ here indicates spectral averaging.
In the presence of a stellar radiation field, the grains will experience a net force, and thus a net torque, from the unidirectional part of the radiation field. This can be accounted for by a factor γ that describes the amount of anisotropy in u_{rad}. The radiation field anisotropy varies between $0 < \gamma \leq 1$. In the diffuse ISM where there is high isotropy $\gamma \simeq 0.1$, in molecular clouds the anisotropy is greater so $\gamma \simeq 0.7$, and near protostars $\gamma \leq 1$.
The torque on the grains due to the unidirectional radiation field will then be [22]

$$\mathbf{\Gamma_{rad}} = \pi a_{\mathbf{eff}}^2 \gamma u_{rad} \frac{\bar{\lambda}}{2\pi} \langle \mathbf{Q_\Gamma} \rangle_\lambda. \tag{2.20}$$

The torque efficiency factor $\mathbf{Q_\Gamma}$ encompasses the different effects the torque will have on the grain as it transfers angular momentum from the radiation field to the grain. This will enable the torque to both dampen or increase $\boldsymbol{J}$, spin up the grains rotation rate, and change the grains orientation.

2.3.2 The dust grain equation of motion

When the grains are internally aligned they will preserve their angular momentum, and their angular velocity can be written as $\boldsymbol{\omega} = \omega \mathbf{\hat{a}}_1$. Because their momentum is preserved, the grains will adapt their motion and position in space to the external torques that affect them

$$\sum_i \mathbf{\Gamma}_i = \mathbf{\Gamma}_B + \mathbf{\Gamma}_{\text{rad}} + \mathbf{\Gamma}_{\text{drag}}, \tag{2.21}$$

namely from the magnetic field, radiation field and from the gas drag. Newton's second law can be written in spherical coordinates as

$$I_1 \cdot \left[\mathbf{\hat{a}}_1 \frac{d\omega}{dt} + \boldsymbol{\hat{\xi}} \frac{d\xi}{dt} + \boldsymbol{\hat{\phi}} \omega \sin(\xi) \frac{d\phi}{dt} \right] = \sum_i \mathbf{\Gamma}_i \tag{2.22}$$

where I_1 is the grains largest moment of inertia along its semi-minor axis $\hat{a}_1$,

$$I_1 = \frac{8\pi}{15} \rho s a^5 \tag{2.23}$$

where $\rho = \rho_{sil}$ is the mass density of the silicate grains. The full grain orientation is presented in Figure 2.4.

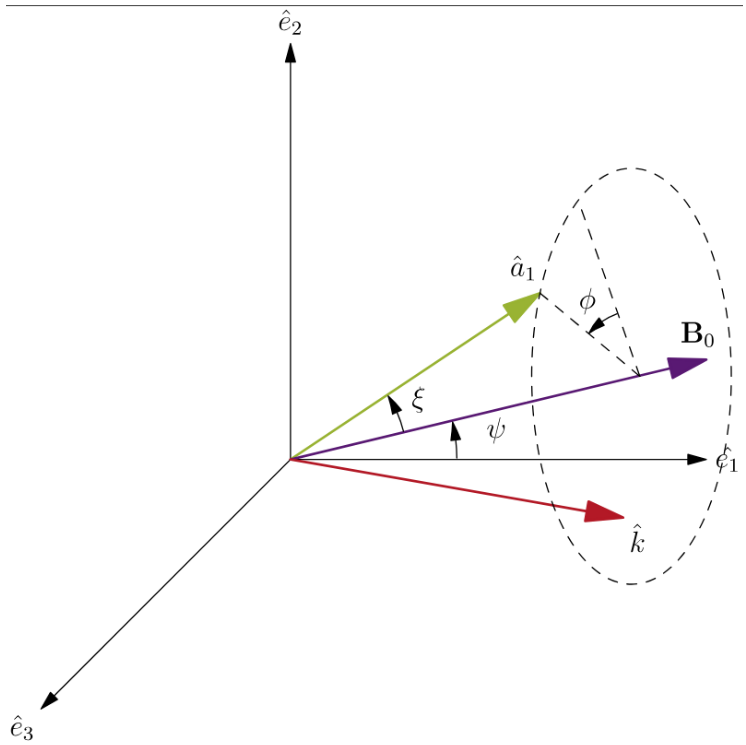

Figure 2.4: Grain orientation showing the grain rotation/alignment coordinates ξ and ϕ. $\mathbf{B}_0$ is the static magnetic field, $\hat{\boldsymbol{k}}$ is the uniform and static radiation field direction, where ψ is the angle between $\mathbf{B}_0$ and $\hat{\boldsymbol{k}}$.

All torques will have some component that is perpendicular to $\boldsymbol{J}$. This component will cause the angular momentum, and by extension the grain's short axis, to precess the external field responsible for the torque. It is the rate of these precessions that will determine which of the external fields the grains will choose to align to. The grains will only end up properly noticing the field that it precesses the fastest, i.e. that has the shortest precession timescale, and will over time align itself to. The alignment to each field are called Radiative Alignment Torques, and are each called B-RAT, k-RAT.
We will now look closer at these candidate torques in turn.

2.3.3 The external alignment torques

In this section the three external torques are presented. First the Barnett induces Larmor precession of grains around a magnetic field (B-RAT), then the radiative precession torque around the radiation field (k-RAT), and finally the torque from random gas collisions causing drag on the grains.

2.3.3.1 B-RAT, Barnett induced Larmor precession

Because the silicate material is paramagnetic, the grains will acquire a magnetic moment when they are spun up. If the grains have a non-zero surface charge, the spinning grain can produce a surface current and thus a magnetic moment that way. There is however a second way the grains can gain an even greater magnetic

moment, from what is called Barnett magnetisation, and relies on the material containing unpaired electrons [23].
The silicate material we model has embedded Fe ions, either Fe^{2+} or Fe^{3+}, that provide unpaired $3d$ electrons. Each electron will have a magnetic moment $\mu = p\mu_B$ where μ_B is the Bohr magneton, and p is the effective moment per iron atom depending on the spin quantum numbers S and L of the electrons in the outer partially filled iron shells [24],

$$p = \sqrt{L(L+1) + 2S(S+1)}. \tag{2.24}$$

The silicates can contain either Fe^{2+} ($^5D_4$) or Fe^{3+} ($^6S_{5/2}$), which have respective effective moments 5.9 and 5.5. It is customary to average to the lower of the two. It's either this, or L is excluded from the calculation, and $p \simeq 4.9$ for Fe^{3+}, and then the average of the two is taken as is.
The grains will be paramagnetic if the material, including the iron atoms, are diffusely distributed in the grains. This type of paramagnetic material will have a susceptibility as given by Curie's law [25]

$$\chi(0) = \frac{n_p \mu^2}{2k_B T_d}. \tag{2.25}$$

where $n_p = f_p\, n_{sil}$ is the number of iron ("paramagnetic") atoms as n_{sil} is the total silicate material number density and $f_p = 7$ is the fraction of iron atoms in the material ($SiMgFeO_4$), k_B is the Boltzmann constant and T_d is the temperature of the dust grains,
When the grain rotates, the free electrons in the material will tend to align their spin with $\boldsymbol{\omega}$ in order to lower the systems rotational energy. This is called paramagnetic relaxation and will produce a net magnetic moment $\boldsymbol{\mu}$ that is both proportional and parallel to the grains angular velocity. This is called Barnett magnetisation, and the final magnetic moment that is induced on an oblate grain of volume $V = \frac{4\pi}{3} s a^3$ is given by

$$\boldsymbol{\mu}_{\mathrm{Bar}} = \frac{\chi(0) V \boldsymbol{\omega}}{\gamma_e} \tag{2.26}$$

where γ_e is the gyromagnetic ratio for electrons. Here, the full expression for the ratio is used,

$$\gamma_e = -g_e \frac{(-e)}{2\, m_e} \tag{2.27}$$

where e is the electron charge, m_e is the electron mass and $g_e \simeq 2.0000470203511$ is the g-factor for electrons (NIST CODATA).
The interaction between the Barnett induced magnetic moment with an external magnetic field $\boldsymbol{B}$ is governed by the torque

$$\boldsymbol{\Gamma}_B = \Big[-\boldsymbol{\mu}_{\mathrm{Bar}} \times \boldsymbol{B} \Big] = -\|\boldsymbol{\mu}_{\mathrm{Bar}}\|\, B \,\sin(\xi)\, \hat{\boldsymbol{\phi}}. \tag{2.28}$$

This torque is along the direction perpendicular to $\boldsymbol{J}$ (see Figure 2.4) and is thus the component in the equation of motion that causes the precession of $\boldsymbol{J}$ around $\boldsymbol{B}$. Excluding all other torques,

$$I_1\,\omega \sin\xi \left(\frac{d\phi}{dt}\right) \hat{\boldsymbol{\phi}}\Big|_B = I_1\,\omega\,\sin\xi\,\boldsymbol{\Omega}_{\mathrm{Lar}}\,\hat{\boldsymbol{\phi}} = \boldsymbol{\Gamma}_B \cdot \hat{\boldsymbol{\phi}} \tag{2.29}$$

The Larmor precession timescale, τ_{Lar}, for the precession of dust grains around the magnetic field $\mathbf{B}$ is thus given by

$$\tau_{\mathrm{Lar}} = \frac{2\pi}{|\boldsymbol{\Omega}_{\mathrm{Lar}}|} = \frac{2\pi I_1 \omega}{\|\boldsymbol{\mu}_{\mathrm{Bar}}\| B}. \tag{2.30}$$

The timescales full variable dependence can be written as

$$\tau_{\mathrm{Lar}} \propto \frac{\rho_{\mathrm{sil}}}{n_{\mathrm{sil}}\, f_p\, p^2}\, \frac{T_d}{B}\, a^2. \tag{2.31}$$

2.3.3.2 k-RAT

As mentioned in Section 2.3.2, the radiative torque will have a component that is perpendicular to the angular momentum $\boldsymbol{J}$. If the precession torque is much stronger than the other external torques, the grain will precess the radiation field $\mathbf{k}$ according to

$$I_1 \cdot \omega\, \sin(\xi)\, \frac{d\phi}{dt} \hat{\boldsymbol{\phi}}\Big|_{\mathrm{rad}} = \boldsymbol{\Gamma}_{\mathrm{rat}} \cdot \hat{\boldsymbol{\phi}} = \Gamma_{\mathrm{k,perc}}, \tag{2.32}$$

where $\Gamma_{\mathrm{k,perc}}$ is the radiative torque component perpendicular to $\boldsymbol{J}$:

$$\Gamma_{\mathrm{k,perc}} = \frac{\gamma\, u_{\mathrm{rad}}\, a_{\mathrm{eff}}^2\, \bar{\lambda}}{2}\, \bar{\boldsymbol{Q}}_{\Gamma} \cdot \hat{\boldsymbol{\phi}} = \frac{\gamma\, u_{\mathrm{rad}}\, a_{\mathrm{eff}}^2\, \bar{\lambda}}{2}\, \langle Q_{e3} \rangle_{\lambda}. \tag{2.33}$$

For unpolarised light, unpolarised light will only produce this third torque component on the spheroid grain, characterised by the third efficiency component Q_{e3}, while the other two vanish (see Chapter 9, Hoang 2007a [26]). Q_{e3} will therefore encompass the entire efficiency of the precession torque and can be expressed as

$$Q_{e3} = \begin{cases} 2.33 \left(\dfrac{\lambda}{a}\right)^{-3}, & \text{for } \dfrac{\lambda}{a} < 1.8, \\ 0.4, & \text{for } \dfrac{\lambda}{a} > 1.8. \end{cases} \tag{2.34}$$

where all and any geometric factors are baked into the efficiency component Q_{e3} [3]. The spectral average of this parameter can be calculated by inserting Q_{e3} from Equation 2.34 into Equation 2.19.

The precession velocity around the radiative field then becomes

$$\omega_{\mathrm{k,perc}} = \frac{\Gamma_{\mathrm{k,perc}}}{I_1\, \omega_{\mathrm{T}}} \tag{2.35}$$

where I_1 is the oblate grains greatest moment of inertia and ω_{T} is the thermal angular velocity

$$\omega_T = \frac{2 k_B T_g}{I_1}. \tag{2.36}$$

The full timescale is then

$$\tau_{k\text{-RAT}} = \frac{2\pi}{\omega_{\mathrm{k,perc}}} = \frac{4\pi I_1 \omega_T}{\gamma\, u_{\mathrm{rad}}\, a_{\mathrm{eff}}^2\, \bar{\lambda}\, \langle Q_{e3}\rangle_\lambda}. \tag{2.37}$$

The k-RAT timescale is often parametrised as simply

$$\tau_k = \frac{2\pi I_1 \omega_T}{\gamma\, u_{\mathrm{rad}}\, a_{\mathrm{eff}}^2\, \bar{\lambda}\, \langle Q_{e3}\rangle_\lambda}. \tag{2.38}$$

This version of the torque was used by Lopez-Rodriguez et al. [27] and Tazaki et al. [9], based on the estimate of the timescale by Lazarian and Hoang in 2007 [26][1]. In this paper, I will use the full expression in Equation 2.37 and have in mind the expected offset by 2 in the upcoming analysis. The full parameter dependence of the radiative torque is this

$$\tau_{k\text{-RAT}} \propto \frac{\rho^{1/2}\, s^{-1/6}\, a^{1/2}\, T_g^{1/2}}{\gamma\, u_{\mathrm{rad}}\, \bar{\lambda}\, Q_{\mathrm{e3}}}. \tag{2.39}$$

2.3.3.3 Gas drag

The gas damping torque describes the rotational drag exerted on the dust grains by collisions with surrounding gas particles. It will compete against the RAT spin-up and determine of the grains can reach suprathermal rotations. As gas atoms and molecules continuously collide with a grain, the collisions remove angular momentum J from the grain and oppose its rotation.

The derivation therefore relies on the Fluctuation-dissipation theorem and that in the absence of other physical processes, the grains will tend to establish thermal equilibrium, T_{eq}. It assumes that the grains rotate thermally and on dividing the derivation into two processes, that the gas particles first stick at collision and then evaporate thermally from the grains. The full two-part derivation was first done by Roberge 1993 (see Appendix A-C [28]).

The rotational damping is written as an exponential decay of the angular momentum

$$\frac{dJ}{dt} = -\frac{J}{\tau_{gas}} \tag{2.40}$$

where τ_{gas} is the damping timescale. The mean torque about the major axis of inertia is in this relation given by

$$\langle \Delta\mathbf{\Gamma}\rangle_{c+ev} = -\mathbf{\Gamma}/\tau_{\mathrm{gas}} \tag{2.41}$$

from which the gas damping time can be derived to be [28]

$$\tau_{\mathrm{gas}} = \frac{2\, I_1 k_B T_{\mathrm{eq}}}{\langle \Delta\mathbf{\Gamma}\rangle_{c+ev}} \tag{2.42}$$

[1] This was confirmed to be just an estimate and not the fully accurate expression for the k-RAT timescale in private communication with Professor Hoang on the 22nd of April, 2026.

where T_{eq} will be the gas temperature T_g. For our grain model, the characteristic damping time of an oblate spheroidal grain for rotation along the parallel direction of the gas flow to the grain symmetry axis $\hat{\mathbf{a}}_1$ is given by

$$\tau_{\rm gas} \equiv \frac{3}{4\sqrt{\pi}} \frac{I_1}{n_{H\,{\rm I}+H\,{\rm II}} m_{\rm gas} v_{\rm th} a^4 \Gamma_{\parallel}} \tag{2.43}$$

where $n_{H\,{\rm I}+H\,{\rm II}}$ is the gas volume density, $m_{\rm gas} = m_H\mu$ is the mean gas mass, and $v_{th} = (2k_B T_g/m_H)^{1/2}$ is the grain thermal velocity. $\Gamma_{\parallel}$ is a geometrical factor dependent on the grain shape factor s.
A parametrised estimate of the timescale is

$$\tau_{\rm gas} \propto \frac{\rho\, s\, a}{n_{H\,{\rm I}+H\,{\rm II}}\, T_g^{1/2}\, \Gamma_{\parallel}}. \tag{2.44}$$

2.3.4 Grain alignment and disruption (RAT-D)

We can assume that the radiation sources have constant luminosity, so that the radiative torques are constant in time. From the equation of motion, this fixes the angular velocity derivative to be constant. The angular velocity will therefore accelerate at a constant pace determined by the radiative torque strength $\Gamma_{\rm RAT}$ and the full gas damping time τ_{damp} [3]

$$\omega_{\rm RAT} = \frac{\Gamma_{\rm RAT}\, \tau_{\rm damp}}{I_1}. \tag{2.45}$$

The damping time will depend on the gas damping derived in Section 2.3.3.3 as well as the dust grains' own rotational damping in the form of infrared (IR) emission. The IR photons will take with them part of the grains' angular momentum. The rotational damping caused by this IR emission can be expressed as a factor $1/F_{\rm IR}$ of the gas damping: $\tau_{\rm IR}^{-1} = F_{\rm IR}\, \tau_{\rm gas}^{-1}$,

$$F_{\rm IR} \simeq 0.4 \left(\frac{u_{\rm rad}}{u_{\rm ISRF}}\right)^{2/3} \left(\frac{a}{10^{-5}{\rm cm}}\right)^{-1} \left(\frac{n_{\rm H}}{30\,{\rm cm}^{-3}}\right)^{-1} \left(\frac{T_g}{100\,{\rm K}}\right)^{-1/2} \tag{2.46}$$

where the terms in parentheses are normalisations of the parameter dependencies [29]. The total damping by gas collisions and excitation of IR photons can therefore be expressed as

$$\tau_{\rm damp}^{-1} = \tau_{\rm gas}^{-1}\,(1 + F_{\rm IR}) \Leftrightarrow \tau_{\rm damp} = \frac{\tau_{\rm gas}}{(1 + F_{\rm IR})}. \tag{2.47}$$

2.3.4.1 Alignment criterion

As was mentioned in Section 2.3.3.3, alignment can first take place when RAT are strong enough to suppress the effects of the damping on the grains. The grains will then leave thermal equilibrium with their environment and reach suprathermal rotation. This criterion can simply be expressed as

$$\omega_{\rm RAT} \gg \omega_{\rm th}. \tag{2.48}$$

where $\omega_{\text{th}} = (k_B T_g / I_1)^{1/2}$. As both velocities depend on the grain size a, the criterion can give a minimum grain size at which the grains are large enough for the RAT spin up to overcome the rotational damping, making it possible for the grains to align, a_{align}. A usual limit at which the spin up is possible is usually set to $\omega_{\text{RAT}} = 3\omega_{\text{th}}$ [3].

2.3.4.2 RAT disruption limit, RAT-D

As the grains spin up they will develop a centrifugal stress $S = \rho a^2 \omega^2 / 4$. The grains will stick together by their internal tensile strength counteracting the stress, which however will have an upper stress limit at which the grains will break apart. We call this maximum stress tolerance limit S_{max}.
As the grains are accelerated by the RAT, they will spin up to a velocity at which the grains can no longer keep together and will disrupt. This disruption velocity limit is given by

$$\omega_{\text{disr}} = \frac{2}{a} \left(\frac{S_{\text{max}}}{\rho} \right)^{1/2}. \tag{2.49}$$

The nature of S_{max} for dust in the ISM is difficult to determine, as the structure and composition of the dust grains likely depends on many factors in their environment. In Lopez-Rodriguez 2024 [27], they estimate that the tensile strength will be weaker in the denser regions of the ISM a due to the turbulent environment, possibly leading to a more complex and unstable composition of the grains. They likewise estimate that the diffuse medium may allow for a more compact and stable composition, and thus a higher tensile strength.
By finding at which grain size a the angular momentum due to RAT exceeds the velocity threshold for disruption, one can estimate a maximum size for grains to be aligned without risking disruption. It will also tell us about the size distribution in that environment.

3

Methodology

This chapter describes the observational data and methods used to study the magnetic-field structure and dust properties of IC 10. Section 3.1 presents the polarimetric data from the Stratospheric Observatory for Infrared Astronomy (SOFIA) and the construction of the polarisation map. Section 3.2 describes the *Herschel* data reduction and modified blackbody fitting used to derive the dust temperature and gas-column-density maps. Section 3.3 describes the radiative alignment torque (RAT) calculations used to estimate the external alignment timescales and grain-size alignment limits introduced in Section 2.3.

3.1 Polarisation vector maps

The magnetic-field morphology of IC 10 was studied using High-resolution Airborne Wideband Camera Plus (HAWC+) polarisation data from the Survey on extragALactic magnetiSm with SOFIA (SALSA; Lopez-Rodriguez et al., 2022 [30]). The dataset has a passband centre in the FIR at 155 µm and covers an area of $8.1' \times 7.6'$ on the sky, with a pixel scale of 6.93 arcsec per pixel (70×66 pixels in total). It therefore traces thermal emission from dust grains. As is commonly assumed that the dust grains are aligned according to B-RAT, the polarisation orientation is perpendicular to the magnetic field direction. The polarisation vectors were therefore rotated by 90°.

The polarisation data were selected using several common but conservative quality cuts [10]. The signal-to-noise ratio of the polarisation flux, P, was required to satisfy $P/\sigma_P \geq 3$, and the debiased degree of polarisation was given an upper limit of $p < 15\%$. Only the polarisation measurements satisfying the adopted signal-to-noise and quality-selection criteria were retained. This filtering was necessary because the HAWC+ coverage of IC 10 contains a limited number of independent polarisation detections, and unreliable vectors can strongly affect the inferred magnetic field morphology. The cut made on the data is shown in Figure 3.1

The final polarisation vector map is shown in Figure 3.1 (right panel) with the polarisation intensity as the backdrop. A corresponding map of the inferred magnetic field orientation (rotated by 90°) is shown against the Stokes I (left panel). These maps are used in the alignment analysis to compare the magnetic field geometry with the dust emission and derived ISM properties.

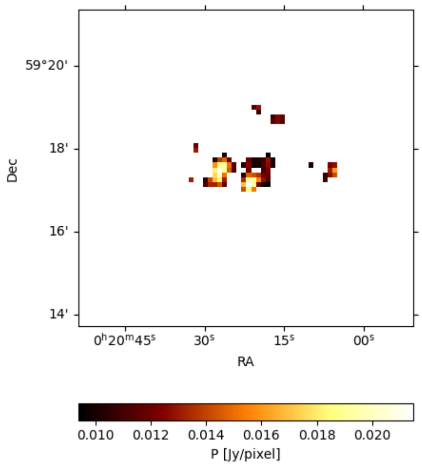

Figure 3.1: The remaining pixels after selection based on the signal-to-noise ratio requirement $P/\sigma_P \geq 3$ and the general polarisation upper degree limit $p < 15\%$.

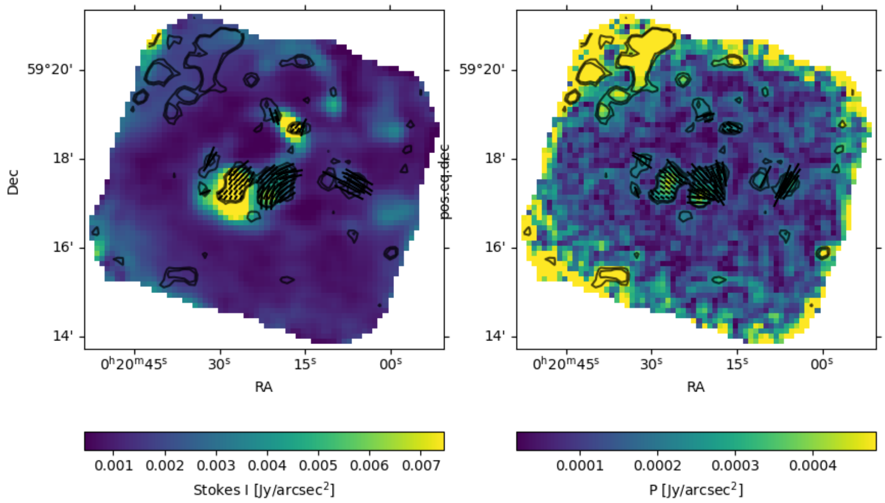

Figure 3.2: Inferred magnetic-field lines (left) and polarisation vectors (right) on IC 10 at 155 µm. The background maps are Stokes I (left) and polarisation flux (right) in units Jy/arcsec^2. The vectors in both maps are selected from the quality cuts of $P/\sigma_P \geq 3$ and $p < 15\%$.

3.2 Deriving dust temperature and column density maps from Herschel observations

To investigate how the magnetic-field structure and dust-grain properties are related to the physical conditions of the interstellar medium (ISM) in IC 10, maps of the dust temperature and gas column density were derived from far-infrared (FIR) observations obtained with *Herschel*. These maps were produced by fitting a modified blackbody (MBB) model to the observed spectral energy distribution (SED) in each pixel.
Section 3.2.1 introduces the Photodetector Array Camera and Spectrometer (PACS) and Spectral and Photometric Imaging Receiver (SPIRE) observations used in the analysis. The data preparation, including unit conversion, convolution to a common angular resolution, and reprojection onto a common grid, is described in Section 3.2.2. The MBB fitting procedure used to derive the dust temperature and gas column density is presented in Section 3.2.3, while the implementation of colour corrections is discussed in Section 3.2.4. The colour corrected intensity maps are then compared with inferred intensities from *Planck* observations in Section 3.2.5 to determine the reliability of the fully prepared data sets. Finally, in Section 3.2.6, the resulting gas column density map is compared with direct measurements of neutral hydrogen from the Karl G. Jansky Very Large Array (VLA).

3.2.1 Herschel PACS and SPIRE observations

The analysis is based on observations obtained with the PACS and SPIRE instruments aboard *Herschel*, covering wavelengths from 70 µm to 500 µm. The maps were downloaded from the Herschel Science Archive. The exact selection is presented in Appendix 7.
For the PACS observations, we used the JScanam maps processed to Level 2.5 in the PACS pipeline [31]. Although Level 3.0 products were also available, the Level 2.5 maps were adopted as they provided science-ready products while avoiding potential large-scale artefacts in the surroundings of the galaxy. Since PACS products from Level 2 onward are considered suitable for scientific analysis, the Level 2.5 maps were deemed sufficient for the present work. A full description of the PACS calibration pipeline is provided in the PACS Products guide [31].
The PACS 160 µm maps are produced in parallel with both of the shorter wavelengths PACS observations. For this analysis, the PACS 160 µm map associated with the 100 µm observation was adopted. The final selected PACS maps are shown in their original frame in Figure 3.3.
For the SPIRE observations, we use the extended-source calibrated maps. These products are labelled short, medium or long (S, M, L) according to their wavelength, with SPIRE covering the bands 250 µm, 350 µm and 500 µm. Level 2 calibrated extended source maps were selected following the suggestion of the "Extended source photometry (starting from extended source maps)" recipe described in Section 5.12 of the SPIRE Handbook [32]. The selected SPIRE maps are shown in their original frame in Figure 3.4
It is worth noting that the Herschel SPIRE 250 µm map shows large-scale diffuse

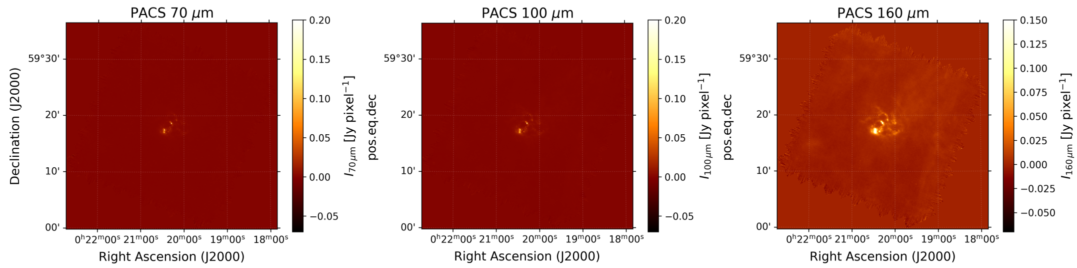

Figure 3.3: Selected Herschel PACS maps of IC 10 at 70 µm, 100 µm, and 160 µm. All maps are Level 2.5 JScanam products. The 160 µm map was selected from the data set of the 100 µm observation.

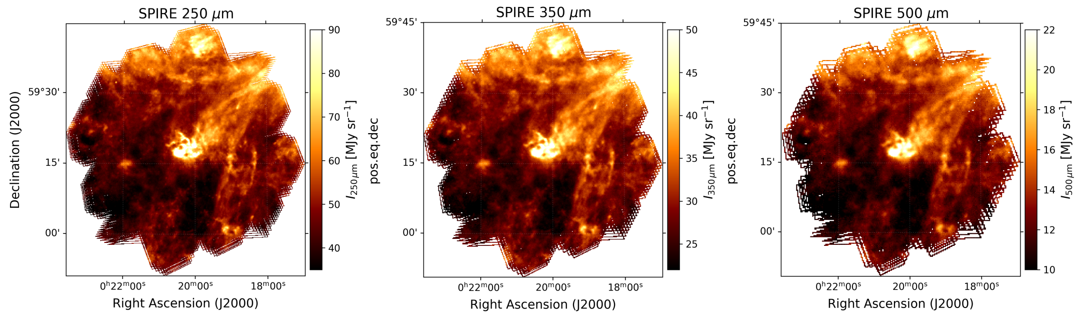

Figure 3.4: Selected Herschel SPIRE maps of IC 10 at 250 µm, 350 µm and 500 µm. The maps are Level 2 extended source calibrated products.

emission around IC 10. This is likely dominated by Galactic foreground contamination from the Milky Way, and is therefore taken into account when assessing the reliability of the derived maps.

3.2.2 Data preparation

The Herschel images cover a field of view larger than the angular extent of IC 10. The data preparation procedure is partly based on the extended source photometry recipe described in Section 5.12.1 of the SPIRE Handbook [32].
The PACS maps were first converted to the same surface-brightness units as the SPIRE maps, from Jy/pixel to MJy/sr. All data sets were then convolved to a common resolution corresponding to the least resolved Herschel band, namely the SPIRE 500 µm map with a full width at half maximum (FWHM) of 36 arcsec .
For the SPIRE maps, their point-spread functions are all approximately Gaussian, so the convolution to the 500 µm resolution could be performed using a two-dimensional Gaussian kernel from the `astropy` package [33]. The PACS point-spread functions are not as well described by simple Gaussian profiles, so these maps were convolved using dedicated convolution kernels designed to convolve each specific PACS beam to the 500 µm beam. The kernels were taken from the Astronomical Convolution-kernel repository and their construction is described by Aniano et al. [34].
As the final preparation step, the Herschel maps were reprojected onto the grid of the SPIRE 500 µm map using the `reproject` Python package [35]. This produced a set of maps with consistent units, angular resolution, and pixel grid. These could then

be used to derive the dust temperature and gas column density through pixel-by-pixel spectral energy distribution (SED) fitting with a modified blackbody (MBB) model.

3.2.3 Modified blackbody fitting

Assuming that the dust is in thermal equilibrium, the far-infrared dust emission could be modelled as optically thin modified blackbody emission. Following Shirley et al. (2026) [36], the specific intensity at a frequency ν, given a reference frequency ν_0, can be written

$$I_\nu = \mathcal{B}_\nu(T_\mathrm{d}, \nu) \left(\frac{\nu}{\nu_0}\right)^\beta \tau_{\nu_0}. \tag{3.1}$$

where $\mathcal{B}(T_d, \nu)$ is the Planck function at dust equilibrium temperature T_d, β is the emissivity index and τ_{ν_0} is the optical depth of the dust at the reference frequency. A suitable model for the optical depth is to express it as the product of the average dust absorption mass opacity κ_{ν_0} and the dust surface density Σ_d

$$\tau_{\nu_0} = \kappa_{\nu_0} \Sigma_d. \tag{3.2}$$

The mass surface density Σ_d is related to the gas column density N_H by a dust-to-gas ratio R_{gd} of the surface densities

$$\Sigma_d = \frac{\Sigma_g}{R_{gd}} = \frac{\mu m_H N_g}{R_{gd}} \tag{3.3}$$

where m_H is the hydrogen atomic mass and μ is the mean gas mass. The gas column density can then be directly related to τ_{ν_0} by

$$N_g = \frac{\Sigma_d}{\mu m_H} R_{gd} = \frac{\tau_{\nu_0} R_{gd}}{\kappa_{\nu_0} \mu \, m_H}. \tag{3.4}$$

The full SED fitting procedure to a modified blackbody in Equation 3.1 is described in the rest of this section. Additional analysis steps are described in the following sections.

The IC 10 has a low metallicity of only 1/4 solar metallicity [12] and so the transition of atomic gas to molecular will require a higher column density than that in the Milky Way. In the Milky Way the transition happens at column densities of a few times $10^{20}\,\mathrm{cm}^{-2}$ [37], and in the IC 10 environment, it will happen at a few times $10^{21}\,\mathrm{cm}^{-2}$ [38]. In the VLA map of the neutral hydrogen gas column density in Figure 3.10, the H I column density is mostly around $10^{21}\,\mathrm{cm}^{-2}$. We therefore assume that the gas is mostly atomic, since it would not be above the H I–H_2 transition column density for low metallicity gas. The mean gas mass is therefore set to $\mu = 1.4$ for atomic gas.

With the Herschel maps with different wavelengths (Figures 3.3 and 3.4), we performed the non-linear least-squares fitting using the `lmfit` package [39]. By converting the wavelengths to corresponding frequencies, we fitted T_d and τ_{ν_0} in Equation 3.1 over the intensities at each set of frequency values for every pixel in the sky map,

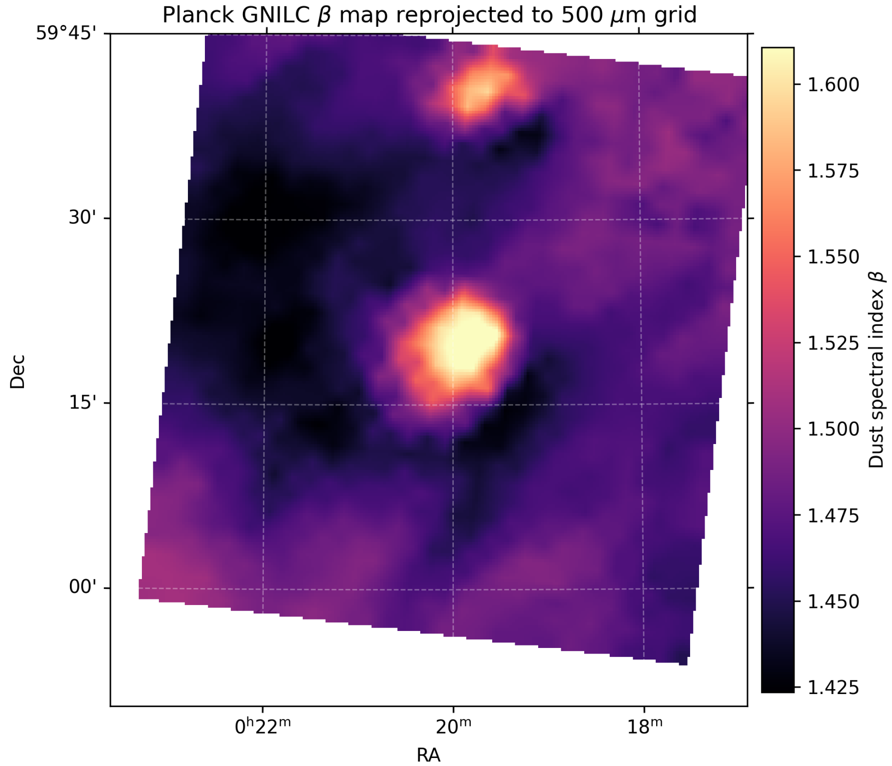

Figure 3.5: The *Planck* Generalized Needlet Internal Linear Combination (GNILC) spectral-index map, β, for IC 10, reprojected onto the Herschel SPIRE 500 µm grid.

keeping β fixed for each pixel. Finally, the gas column density could be retrieved using Equation 3.4. For this work, the adopted reference frequency was $\nu_0 = 1000\,\mathrm{GHz}$ and the opacity was set to that of the Milky Way dust, $\kappa_{\nu_0} = 10\,\mathrm{cm}^2\,\mathrm{g}^{-1}$ (see Shirley et al. [36], Figure 12). The gas-to-dust ratio in IC 10 is $R_{\mathrm{gd}} = 475$ [40].
The thermal dust emission continuum has earlier been modelled as a modified blackbody spectrum. Early works with low resolution data showed indications of an unusually low emissivity index $\beta \sim 0.5$ [41]. However, when the co-existence of cold and warm dust components was taken into account, it was shown that the data are compatible with a more usual spectral index of 1.5. Another study assumed a typical value of 2 [17]. In this work, we use the estimates of β from the *Planck* spectral index map, reprojected onto the SPIRE 500 µm grid (see Figure 3.5). Where the Planck map did not overlap with the Herschel maps, a default value of 1.5 was set.

3.2.4 Colour correction of Herschel fluxes

The SPIRE handbook [32] and PACS Explanatory Supplement [42] note that additional calibrations need be made on the science-ready data, when fitting the data to for example a modified blackbody.
The Herschel bolometers measure the flux density $\bar{S}_S$ as the integral over the relevant passband of the incident flux density weighted by the telescopes relative spectral response function $R(\nu)$ and the aperture efficiency $\eta(\nu)$,

$$\bar{S}_S = \frac{\int_{Passband} S_S(\nu) R(\nu)\eta(\nu) d\nu}{\int_{Passband} R(\nu)\eta(\nu) d\nu} \tag{3.5}$$

where $S_S(\nu)$ is the in beam source flux density at the telescope aperture and incident frequency ν. The Herschel pipeline assumes from here that the source flux density is point-like, with a spectral index $\alpha_{pip} = -1$, and at each passband,

$$I_{pip}(\nu) = I_{pip}(\nu_0) \left(\frac{\nu}{\nu_0} \right)^{\alpha_{pip}} \tag{3.6}$$

for a reference frequency ν_0 corresponding to the frequency at the passband centre. In order to fit the SED of a modified blackbody, the fluxes at each pixel need to be "colour corrected" to follow the pattern of the assumed SED. For a modified blackbody as in Equation 3.1, the intensity can be approximated to $I_S \simeq \nu^\beta \mathcal{B}(T, \nu)$, and so the colour correction for the extended source $K_{ColE}(T, \beta, \nu_0)$ is derived by

$$K_{ColE}(T, \beta, \nu_0) = \nu_0^{\beta - \alpha_{pip}} \mathcal{B}(T, \nu_0) \times \left[\frac{\int_{Passband} \nu^{\alpha_{pip}} \cdot R(\nu)\eta(\nu)\Omega_{eff}(\nu)\, d\nu}{\int_{Passband} \nu^\beta \mathcal{B}(T, \nu) \cdot R(\nu)\eta(\nu)\Omega_{eff}(\nu)\, d\nu} \right] \tag{3.7}$$

where $\Omega_{eff}(\nu)$ is the frequency dependent solid angle used for extended source calculations. The colour corrected intensities are then retrieved by multiplying the correction factor for that mbb of a specific T_d and β to the point-like intensity given in the science-ready data set at the passband centre frequency ν_0,

$$I_{MBB}(\nu_0) = K_{ColE}(T, \beta, \nu_0) I_{pip}(\nu_0). \tag{3.8}$$

The SPIRE Handbook provides the full list of colour corrections for fitting the SPIRE data to modified black bodies of different temperatures and spectral index in Chapter 5.12.3 Table 5.8 [32]. The equivalent PACS data colour corrections are provided in its own catalogue for PACS Colour Corrections in Section 4.3 Table 3 [43]. The PACS colour corrections must be divided to the intensities, unlike how they are multiplied for the SPIRE data.

The colour corrections were added when fitting the SED in the following manner: First an initial MBB was fitted to the data, giving an indicator to the dust temperature at that pixel. The spectral index was taken from the Planck GNILC map (see Figure 3.5), so the colour corrections for the SPIRE and PACS bands respectively could be picked and applied to the initial intensities. Then a new MBB fit was made on the colour corrected Herschel intensities, giving a final temperature and opacity map of IC 10.

Several MBB fitting configurations were explored using different combinations of the SPIRE and PACS data sets. The inclusion of the PACS bands significantly affected the inferred gas column density distribution, motivating a comparison between fits performed with and without PACS data. The dust temperature and gas column density from the MBB fit using the Herschel SPIRE maps and only the PACS 160 µm map from the PACS 100 µm file are shown in Figure 3.6, and the same properties from a fit using only the Herschel SPIRE data is presented in Figure 3.7.

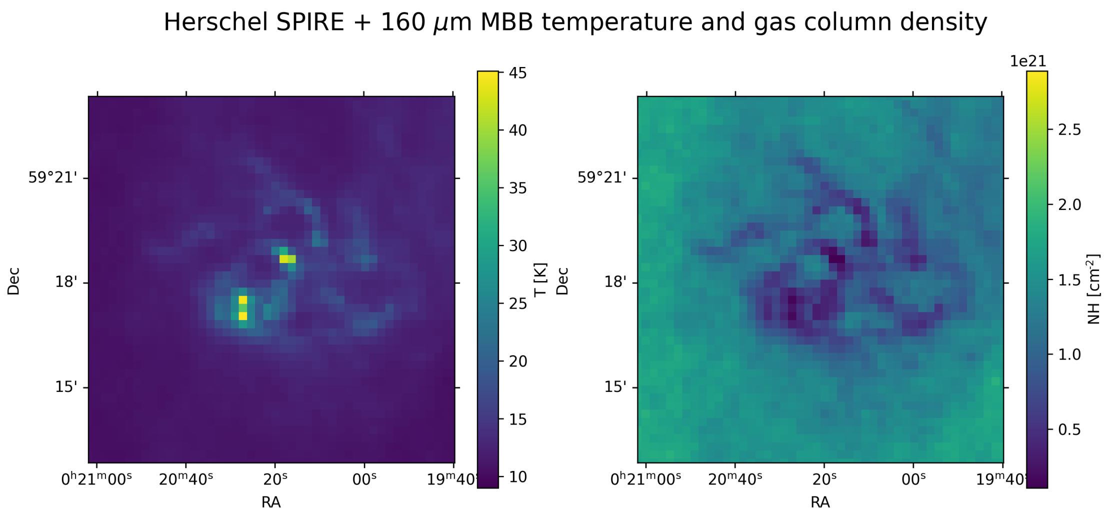

Figure 3.6: Dust temperature (left) and gas column density (right) of IC 10 inferred by MBB SED fitting with colour corrections on the Herschel SPIRE data and the 160 µm PACS map.

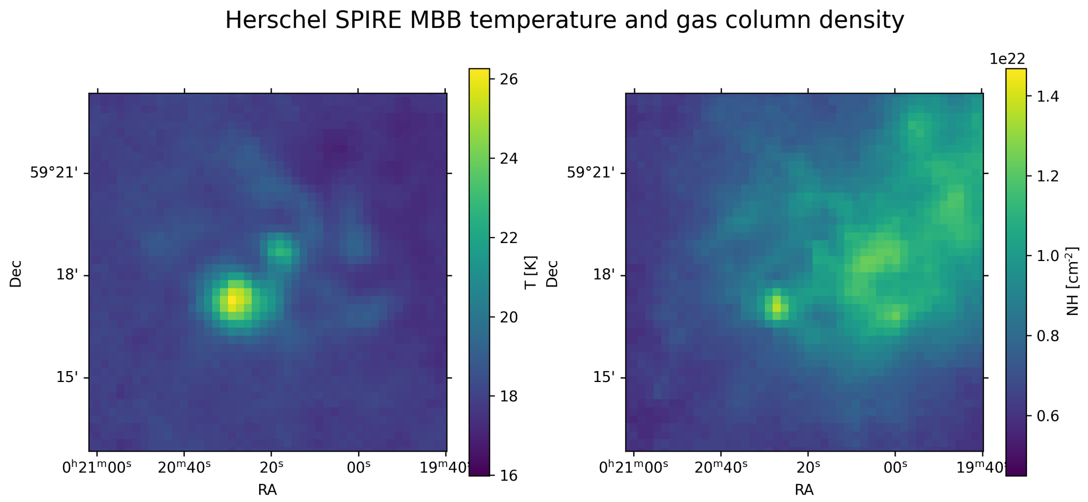

Figure 3.7: Dust temperature (left) and gas column density (right) of IC 10 inferred by MBB SED fitting with colour corrections on the Herschel SPIRE data, of wavelengths 250 µm, 350 µm and 500 µm.

An investigation of the nature of the PACS and SPIRE maps with regard to their background absolute intensity, and their intensity gradient in relation to the Planck observations of IC 10 is presented in the following section.

3.2.5 Absolute intensity calibration and zero-offset correction

The *Herschel* SPIRE and PACS bolometers only provide the relative photometry, but the absolute value of the maps, based on the intensity of the background, needs to be adjusted to a common baseline.

The SPIRE maps are pre-calibrated to a common baseline using data from the Planck telescope [44] as reference for the absolute flux level. A full description of how this has been done is given in the SPIRE Handbook, Chapter 5.10 [32]. The PACS maps are however not standardised in any way (see PACS Products Explained Ch 11.2 [31]). In order to obtain the absolute fluxes of the PACS data maps, and fit the offset to the Planck and SPIRE maps, we used the data from the Planck telescope and followed the method used by Lombardi et al. [45] (Sec. 3.3).

Using the Planck optical-depth, temperature and spectral index maps for IC 10, the expected fluxes at each Herschel passband could be computed using the modified blackbody model presented in Section 3.2.3. The Herschel maps were then correlated using the preparation procedure in Section 3.2.2 to fit the grid and resolution of the Planck maps, with a resolution of 5 arcmin [44].

Each of the Herschel PACS and SPIRE data fluxes were then linearly fitted to the corresponding Planck expected fluxes of that wavelength according to

$$I_E(\nu)_{\textit{Herschel-band}} = a_\nu + b_\nu I(\nu)_{\textit{Planck}}, \tag{3.9}$$

where $I_E(\nu)_{\textit{Herschel-band}}$ is the spectral intensity from PACS and SPIRE at the passband centre ν, $I(\nu)_{\textit{Planck}}$ is the inferred spectral intensity from Planck, b_ν is the slope and a_ν is the offset between the fitted maps. The linear regression of the PACS colour corrected data, from fitting all Herschel fields to a common MBB, to the computed expected fluxes from the Planck maps are shown in Figure 3.8. A comparison with the correlation between the SPIRE data, colour corrected from a MBB fit based on only the SPIRE data, and the inferred Planck fluxes are shown in Figure 3.9.

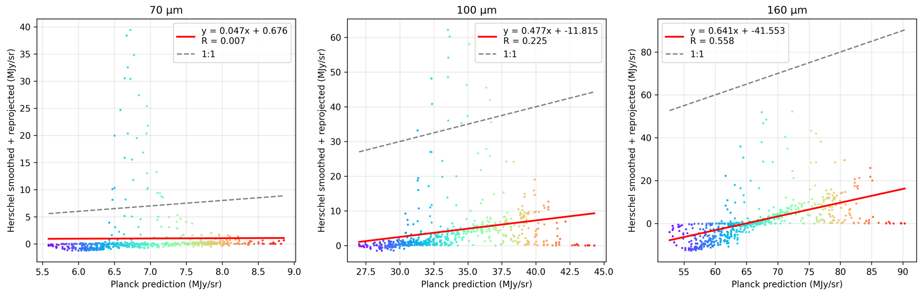

Figure 3.8: Linear regression fits of the PACS colour corrected data in fitting all Herschel PACS and SPIRE maps to a MBB of reference frequency $\nu_0 = 1000\,\text{GHz}$, against the inferred fluxes at the Herschel wavelengths from a MBB fit of the Planck data at reference frequency $\nu_0 = 353\,\text{GHz}$. The red lines show the best-fit linear regression and the dashed black line shows would-be perfect 1:1 agreement. R is the Pearson correlation coefficient.

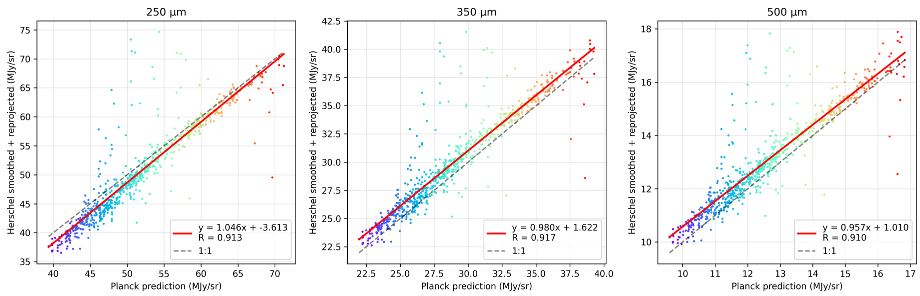

Figure 3.9: Linear regression fits of the SPIRE colour corrected data in fitting only the Herschel SPIRE maps to a MBB of reference frequency $\nu_0 = 1000\,\text{GHz}$, against the inferred fluxes at the Herschel wavelengths from a MBB fit of the Planck data at reference frequency $\nu_0 = 353\,\text{GHz}$. The red lines show the best-fit linear regression and the dashed black lines show would-be perfect 1:1 agreement. R is the Pearson correlation coefficient.

From Figure 3.9, we see that SPIRE and Planck follow a common slope very close to unity, and that the absolute offset has been compensated for, with a_ν being no more than 5 MJy. For the PACS files, however, the offset varies with values up to 41.5 MJy. More importantly, their relative intensities, as indicated by the values of b_ν, are nowhere near 1. This means that the Planck and PACS bolometers computed very different relative intensities, and due to the spread of the PACS data, it becomes difficult to determine a slope. We therefore determined that the PACS data were unreliable for MBB fitting and only used the SPIRE data to acquire the dust temperature and gas column density maps. These maps are presented in Figure 3.7.

The N_H map created from the SED fits to only the SPIRE data shows a physically reasonable trend of the column density, as the density increases towards the centre instead of dropping. The final gas column density map in Figure 3.7 is compared to the direct measurement of neutral hydrogen in IC 10 with the VLA in the following section.

3.2.6 Comparison with VLA H I observations

The procedure and assumptions used to derive the gas column density in IC 10 from Herschel dust emissions are described in Section 3.2. The resulting hydrogen column density map (N_{H}) can be compared to direct observations of neutral atomic hydrogen obtained via 21 cm line emission. The neutral hydrogen (H I) map used in this comparison is based on observations from the Karl G. Jansky Very Large Array (VLA; [46]). The integrated 21 cm brightness temperature is converted to H I column density using the standard relation

$$N_{\mathrm{HI}}\,[\mathrm{cm}^{-2}] = 1.823 \times 10^{18} \int T_b\, dv\ [\mathrm{K\,km\,s^{-1}}],$$

which corresponds to a linear conversion factor of $1.823 \times 10^{18}\,\mathrm{K} \cdot \mathrm{km/s} \rightarrow 1\,\mathrm{cm}^{-2}$. Figure 3.10 presents a side-by-side comparison of the H I column density map derived from the VLA observations and the Herschel-based dust modelling prediction.

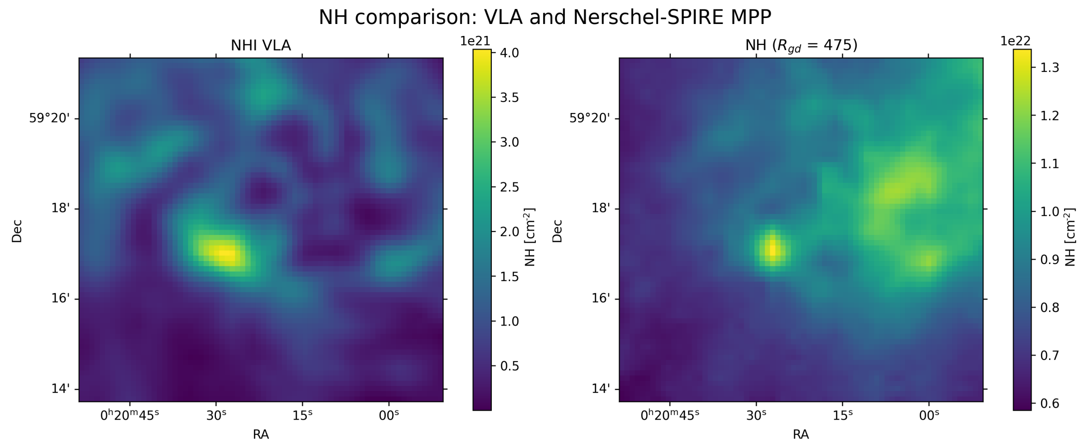

Figure 3.10: Neutral hydrogen column density directly measured from VLA 21 cm observations (left) and indirectly inferred from Herschel dust emission (right). Both reprojected onto the HAWC+ grid.

The VLA map shows a more pronounced spatial structure, with a peak in the middle of the map. In contrast, the Herschel-based map exhibits a broader spatial distribution reaching up toward the top right and a less sharply defined central peak, though it is perceivable.

This is likely due to contamination in the Herschel data from the Milky Way, as its bright and diffuse structure strongly suggests being the Milky Way foreground. We therefore assume that our method overestimates the gas column density due to the presence of Milky Way contamination. One way of estimating the level of Milky Way contamination is to assume a constant level of N_H contributed by the foreground (as a lower limit on the contamination). We notice that in the bottom left part of the map, there is very little HI emission from IC10, thus any signal in

the NH map from Herschel is likely dominated by the Milky Way. The values of the NH map there are $\sim 0.7 \times 10^{22}\mathrm{cm}^{-2}$. If we subtract this level from the entire map, we get values of the N_H map closer to those of the NHI map. For example, in the bright center of IC10, the foreground-subtracted N_H becomes $\sim 0.6 \times 10^{21}$, much closer to the NHI level of 4×10^{21} in the VLA map.
The levels of NHI imply that the gas is likely mostly atomic rather than molecular. Indeed, the transition from atomic to molecular gas happens at column densities of a few $10^{21}\mathrm{cm}^{-2}$ in low metallicity environments [38]. The presence of CO (a molecular gas tracer) is detected only in isolated clumps, not widely over the map (cite VLA paper again). For these reasons, it is reasonable to expect that the NHI map from the VLA is a good tracer of the total column density of IC10. We thus use the VLA NHI map as a proxy for NH in the RAT timescale analysis. We use the dust temperature map from our Herschel analysis, as it shows clear morphology associated with IC10. For this reason, we retain the assumption that the gas in the IC 10 ISM is atomic, and use the H I map from VLA as a proxy for N_H in the RAT time scale analysis, keeping only the T_d map from the MBB fitting.

3.3 RAT timescales and characteristic grain sizes

This section describes the methodology used to evaluate the grain alignment and grain disruption processes in M51 and IC 10. The general procedure and the definitions of the environmental regions considered in the analysis are introduced in Section 3.3.1. Section 3.3.2 presents the adopted input parameters and relevant assumptions that have been made, and Section 3.3.3 describes the implementation of the timescale calculations and the procedure for determining the characteristic alignment and disruption grain sizes in each environment.

3.3.1 General analytical procedure and environment definition

The theoretical analysis follows the methodology of Lopez-Rodriguez & Tram (2024 [27], hereafter LR24), who evaluated grain alignment timescales in the face-on spiral galaxy M51. In their study, M51 was divided into three environmental regions consisting of two spiral-arm regions and one interarm region. The galactic centre was masked out entirely. The relevant physical quantities were evaluated independently in each region, and they assumed the silicate dust grain model with the composition $SiMgFeO_4$.

In this work, the timescale calculations for M51 from LR24 were first reproduced as a validation step. The environmental parameters were estimated from the presented field maps in the LR24 paper, and from tabulated median values from their references. Although the approximations used do not capture the full spatial complexity in the original analysis, they were sufficient to recover the overall behaviour of the published timescales in M51. The full parameter selection for the M51 timescale reproduction is described in Section 3.3.2 and presented in Table 3.3. After validating the reproduction of the M51 results, the corresponding calculations were applied to IC 10.

Two environmental regions were defined based on the HAWC+ polarisation observations made in Section 3.1, Figure 3.1. The pixels with trustworthy polarisation were used as mask for defining a central region where alignment is observationally confirmed. The remaining pixels were assigned to a surrounding region representing the broader galactic environment. These masks, applied to the dust temperature and VLA neutral hydrogen density maps, are shown in Figure 3.11.

Pixels containing non-finite values in any of the required environmental maps were excluded from the calculations. All statistics were computed only from valid pixels

3.3.2 Input parameters and assumptions

An overview of the timescales and angular velocities along with their main and full parameter dependencies, used for the timescale calculations and numerical size limit calculations, are summarised in Table 3.1. The silicate dust grain model and alignment related parameters that were adopted in the calculations for both the replication of M51 and corresponding analysis of IC 10 are listed in Table 3.2.

The M51 input parameters used for reproducing each of the three M51 environments

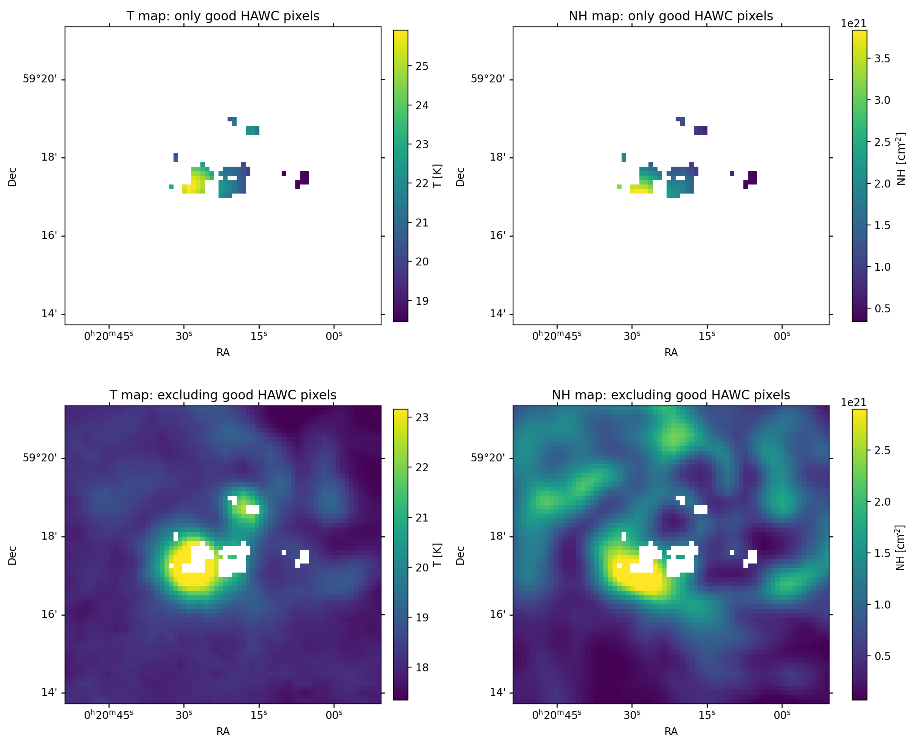

Figure 3.11: The polarisation masking applied to the dust temperature (left) and the gas column density estimate (right) of IC 10. The top row masks the centre environment and the bottom row shows the masked region of the surrounding environment.

in [27] are listed in Table 3.3. Magnetic field strengths and dust temperatures were estimated from their Figure 1, while gas column densities were adopted from Table 3 in their source, Borlaff et al. [4]. The radiation field energy density was calculated from these values using Equation 3.11. Gas temperatures were directly taken from Appendix A in LR24. Some quantities were fixed across all regions, while others were varied between regions for a number of pixels simulating the original map sizes (approximately 80 × 80 pixels). These choices are described in the parameter summary table.

In star forming clouds, such as IC 10, the intense star light can be assumed to exclusively heat up the grains [22]. The energy density that is emitted by the stars can then be estimated by how warm the dust grains are

$$u_{rad} = \left(\frac{T_d}{16.4\,\mathrm{K}}\right)^6 u_{\mathrm{ISRF}} \tag{3.10}$$

where $u_{\mathrm{ISRF}} = 8.64 \times 10^{-13}\,\mathrm{erg\,cm^{-3}}$ is the energy density of the local interstellar radiation field (ISRF), which can heat silicate grains to 16.4 K [18].

Following Lopez-Rodriguez, in spiral arms like M51 the energy density can instead be estimated in the optical to FIR emission,from the column density $N_{H\,\mathrm{I}+H\,\mathrm{II}}$ by the Kennicutt-Schmidt relation

Quantity	Main dependences
Larmor time (B-RAT)	$\tau_{\rm Lar} \propto \frac{T_d\, a^2}{B}$
Radiative precession (k-RAT)	$\tau_{\rm k-RAT} \propto \frac{T_g^{1/2}\, a^{1/2}}{\gamma\, u_{\rm rad}\, Q_{e3}}$
Gas damping	$\tau_{\rm gas} \propto \frac{a}{n_{\rm H}\, T_g^{1/2}}$
RAT velocity, constant spin up	$\omega_{\mathbf{RAT}} \propto \frac{\gamma\, u_{\rm rad}\, Q_{e3}}{a^4\, n_{\rm H}\, T_{\rm g}^{1/2}\,(1{+}F_{\rm IR})}$
Thermal angular velocity	$\omega_{\mathbf{th}} \propto \frac{T_{\rm g}^{1/2}}{a^{5/2}}$
Disruption velocity threshold	$\omega_{\mathbf{disr}} \propto \frac{S_{\rm max}^{1/2}}{a}$

Table 3.1: Summary of the main timescales discussed in the M51 grain alignment analysis, and the angular velocities used in [3] to numerically calculate the grain size limits.

$$u_{\rm rad} = 3 \times 10^{-9} \left(\frac{m_p \mu N_{H\,\rm I + H\,\rm II}}{u_{\rm ISRF}} \right)^{N_{KS}} {\rm K} \tag{3.11}$$

where μ is the mean molecular weight per hydrogen atom, m_H is the hydrogen atom weight, and $N_{KS} = 1.4$ [27].

The value of the radiative torque efficiency adopted by LR24 is not explicitly stated. During the reproduction of their M51 timescale results, a value of $Q_{e3} = 0.01$ was found to give the closest agreement with the published k-RAT timescales[1]. This value was therefore adopted for the M51 reproduction. In addition, a wavelength-averaged grain-size-dependent radiative torque efficiency, $\langle Q_{e3}(a)\rangle_\lambda$, was calculated using Equation 2.19. This prescription was used to investigate the sensitivity of the alignment and disruption grain-size limits to the radiative torque efficiency. For IC 10, both $Q_{e3} = 0.01$ and the wavelength-averaged efficiency $\langle Q_{e3}(a)\rangle_\lambda$ were considered. The former allows direct comparison with the M51 reproduction, while the latter provides a physically motivated estimate based on the full radiation spectrum. Figure 3.12 shows the total local interstellar radiation field energy-density spectrum and the spectral average of the radiation torque efficiency factor.

The tensile strength of the grains was assumed in LR24 to depend on the local environment. In their analysis, denser spiral arm regions were assigned a lower tensile strength, corresponding to grains with a more porous internal structure, while the diffuse interarm medium was assigned a higher tensile strength corresponding to more compact grains. For the IC 10 analysis, a conservative value of

$$S_{\rm max} = 10^7\,{\rm erg\,cm^{-3}}$$

was adopted throughout. This choice yields a smaller estimate of the disruption

[1]This value was confirmed in private communication with Asso. Prof. E. Lopez-Rodriguez on 8th of June, 2026.

Parameter	**Symbol**	**Value / expression**
Silicate grain material properties		
Grain composition	–	$MgFeSiO_4$
Mass density	ρ_{sil}	3.81 g cm^{-3}
Atomic density	n_{sil}	1.33×10^{22} cm^{-3}
Mass per grain	m_{sil}	2.86×10^{-22} g
Paramagnetic fraction	f_p	1/7
Magnetic moment factor	p	$\simeq 5.5$
Grain geometry		
Grain size	a	Semimajor axis
Minor axis	c	Semiminor axis
Axial ratio	s	$s = c/a$
Effective grain size	a_{eff}	$a_{eff} = s^{1/3}a$
Grain volume	V	$V = \frac{4}{3}\pi s a^3$
Moment of inertia	$I_{\parallel}$	$I_{\parallel} = \frac{8}{15}\pi \rho s a^5$
RAT and disruption parameters		
RAT efficiency	Q_{e3}	Varied; see text
Normalized RAT efficiency	$Q_{e3,-2}$	$Q_{e3}/10^{-2}$
Mean radiation wavelength (ISRF)	$\bar{\lambda}$	1.2 μm
IR damping parameter	F_{IR}	Calculated from local radiation field and gas properties
Tensile strength (arms)	S_{max}	10^7 erg cm^{-3}
Tensile strength (interarms)	S_{max}	10^9 erg cm^{-3}

Table 3.2: Dust grain material, geometric, and RAT-related parameters adopted in the grain-alignment calculations.

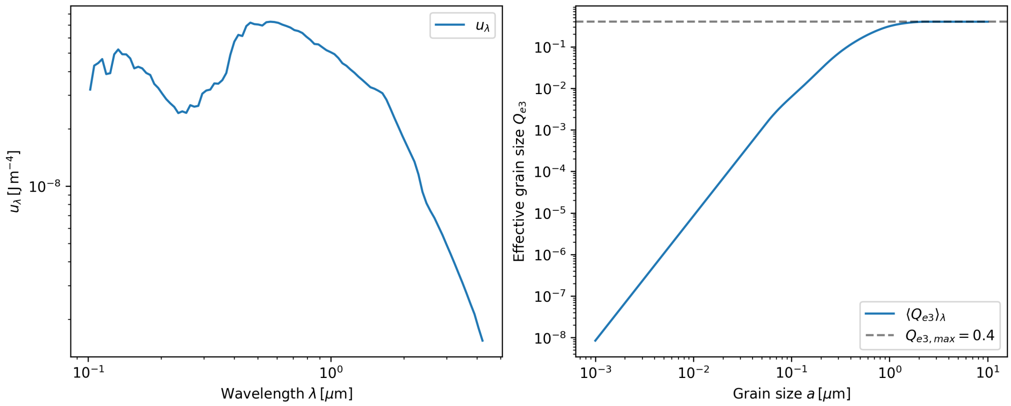

Figure 3.12: The total local interstellar radiation field energy-density spectrum u_λ (data from Bianchi et al 2024 [2]) and the spectral average of the radiation torque efficiency factor $\langle \mathbf{Q_\Gamma} \rangle_\lambda$.

grain size, putting an intentionally tighter upper limit on the alignment sizes in both regions.

The gas volume density was estimated in the M51 by dividing the column density by the vertical height of the galactic disk $h = 200\,\mathrm{pc}$.

For IC 10, the gas volume density was estimated from observational constraints. Carbon monoxide (CO) emission is observed near the peak of the H I distribution (Figure 4 of Leroy et al. [15]), indicating that gas densities there are sufficient for collisional excitation of the CO transition. A volume density of

$$n_\mathrm{H} = 100 \text{ cm}^{-3}$$

was therefore adopted for the central region. In the surrounding environment, the volume density was allowed to vary uniformly between 1 and 100 cm^{-3} in order to reflect the broader variation outside the central star-forming region.

3.3.3 Calculation of timescales, and alignment and disruption grain sizes

For each environment, the RAT timescales were calculated at every pixel in the input maps as a function of grain size, a. The resulting distributions were summarised by the median value at each grain size together with the 16th and 84th percentiles. These percentiles are used throughout this work as a measure of the spatial variation within each environment.

In LR24, an additional uncertainty was included in the calculation of the Larmor precession timescale by varying the magnetic susceptibility, $\chi(0)$, over the range 4.2×10^{-5}–4.2×10^{-3}. The resulting uncertainty combined in quadrature with the uncertainty arising solely from the environmental parameters. In the present work, $\chi(0)$ is not varied independently. Instead, its variation is included through its dependence on dust temperature, as described by Equation 2.25. Since this dependence is already incorporated into the calculation of the Larmor precession timescale

Parameter	**Arm 1**	**Arm 2**	**Interarm**	**Source / note**
B (μG)	17	14	10	Estimated from LR24 Fig. 1.
T_d (K)	18–26	18–26	18–26	Estimated from LR24 Fig. 1.
T_g (K)	T_d	T_d	200	Values adopted by LR24.
$\log_{10}(N_{\rm H})$	21.66	21.49	21.40	Median values from Borlaff et al. (2021), Table 3.
u_{rad} ($/u_{\bf ISRF}$)	15.71	9.547	6.805	Median values calculated using Eq. 3.11.
n_H (cm^{-3})	7	5	4	Computed assuming disk height $h = 200$ pc.
γ	0.8	0.7	0.1	Assumed.
Q_{e3}	0.01	0.01	0.01	Chosen to reproduce LR24 results.
$S_{\rm max}$(erg/cm^3)	10^7	10^7	10^9	Values adopted by LR24.

Table 3.3: Input parameters adopted for the reproduction of the M51 analysis by LR24.

Parameter	**Central region**	**Surrounding region**	**Source / note**
B (μG)	14 µG	1–10 µG	From Chyży et al. [47] and assumed.
$T_d(K)$	19–26	18–23	Derived from Herschel SPIRE MBB fitting.
$T_g(K)$	$T_g = T_d$	50–200	Assumed.
$\log_{10}(N_{\rm H})$	20.70–21.54	20.00–21.46	Derived from VLA H I observations.
$u_{rad}(/u_{\bf ISRF})$	5.381	1.857	Median values from applying Eq. 3.10
n_H (cm^{-3})	100	1–100	Estimated from results in Leroy et al. [15].
γ	0.8	0.1	Assumed.
Q_{e3}	0.01 and $\langle Q_{e3}(a)\rangle_\lambda$	0.01 and $\langle Q_{e3}(a)\rangle_\lambda$	For tests of different efficiency assumptions.
$S_{\rm max}$(erg cm^{-3})	10^7	10^7	Conservative disruption limit.

Table 3.4: Input parameters adopted for the IC 10 grain-alignment calculations. The central region corresponds to the area with reliable HAWC+ polarisation detections, while the surrounding region represents the remaining area of the galaxy (Figure 3.11).

(Equation 2.31), no additional uncertainty is added from $\chi(0)$ to the calculation of B-RAT.
The resulting timescale estimates for the M51 replication and IC 10 are presented in Section 4.2. The exact M51 precession timescale reproduction is shown in Figure 4.1 and an additional presentation of the M51 timescales, but with k-RAT dependent on $\langle Q_{e3}(a)\rangle_\lambda$, is given in Figure 4.2. The IC 10 results are shown in Figure 4.3.
The minimum grain size that can be efficiently aligned, $a_{\rm align}$, was determined using the alignment criterion introduced in Section 2.3.4.1,

$$\omega_{\rm RAT} > 3\,\omega_{th}. \tag{3.12}$$

where $\omega_{\rm RAT}$ is the angular velocity induced by radiative torques and $\omega_{\rm th}$ is the thermal angular velocity. Likewise, the disruption grain size, $a_{\rm disr}$, was defined as the grain size at which the radiative-torque angular velocity exceeds the critical angular velocity for centrifugal disruption,

$$\omega_{\rm RAT} > \omega_{\rm disr}. \tag{3.13}$$

To determine these characteristic grain sizes for each of the environments, the angular velocities $\omega_{\rm RAT}$, $\omega_{\rm th}$ and $\omega_{\rm disr}$ were calculated at every pixel as functions of grain size. For each pixel, the grain size at which the relevant crossing condition was first satisfied was identified by interpolation between neighbouring grain-size samples. This method produced maps of $a_{\rm align}$ and $a_{\rm disr}$ over each of the environments. For each pixel, only the first crossing satisfying the relevant condition was kept. These correspond to the minimum grain size for efficient alignment and the maximum grain size that can survive radiative torque disruption.
The spatial distributions of $a_{\rm align}$ and $a_{\rm disr}$ were then summarised by taking the median values together with the 16th and 84th percentiles. The uncertainties capture the spatial variation across the environments.
To investigate alignment and disruption thresholds dependence on the radiative torque efficiency, Q_{e3}, the RAT angular velocity was computed with three cases of varying Q_{e3}. These were the interpreted value 0.01 from LR24, the maximum value for the efficiency 0.4 and $\langle Q_{e3}(a)\rangle_\lambda$.
The results of these numerical calculations are presented in Section 4.3. The estimated characteristic grain sizes for the M51 environments are shown in Figure 4.4 and 4.5, and the ones for the IC 10 environments in Figure 4.6. The characteristic grain sizes found by applying $\langle Q_{e3}(a)\rangle_\lambda$ were added to the timescale results for M51 in Figure 4.1 and 4.2, and for IC 10 in Figure 4.3.

4

Results

This chapter presents the numerical and analytical results of the methods presented in Section 3. First, Section 4.1 summarises the results from the Herschel fitting described in Section 3.2. Section 4.2 presents the RAT alignment timescales, first the reproduction of M51 from LR24 [27] and then the implementation of the methodology into IC 10. Section 4.3 then presents grain-size limits from the numerical calculations of the thresholds for M51 and IC 10.

4.1 MBB-derived dust properties and adopted ISM maps

From the SED fitting procedure of the Herschel PACS and SPIRE band maps, the final dust temperature map was selected from the product of the colour corrected modified blackbody fitting of the SPIRE maps only. We found that SPIRE and Planck agreed well after the correction (see Figure 3.9), with slopes close to unity and small offsets of only a few MJy, while PACS showed large offsets and non-unity slope (see Figure 3.8) so that they couldn't be easily calibrated. Therefore, the PACS maps were judged to be unreliable for the final MBB fit, and the final maps were based only on SPIRE.

This SPIRE-only MBB fitting produced a dust temperature map with temperatures of approximately $19 - 26\,\mathrm{K}$ in the IC 10 centre region, and $18 - 23\,\mathrm{K}$ in the surrounding region. The map was used to estimate the radiation field energy density map entering the RAT calculations according to Equation 3.10.

The MBB fitting also produced a dust-based gas column density map. However, a comparison with the VLA H I observations presented in Figure 3.10 showed that the Herschel derived N_H turned out more extended and less centrally peaked. This is likely due to Milky Way foreground contamination, that is clearly seen in the original SPIRE maps in Figure 3.4. For this reason, only the MBB-derived T_d map was retained for the RAT analysis, while the VLA H I map was adopted as an estimate for the gas column density.

4.2 Timescale comparison

As a validation test, the M51 timescales from LR24 [27] were reproduced using the approximate regional input values described in Section 3.3.2, and presented in Table 3.3. The resulting timescales are shown in Figure 4.1 together with the derived characteristic alignment and disruption grain size limits.

The reproduced M51 timescales recover the overall ordering and grain size dependence reported by LR24, although it does not capture the full uncertainty from the environments. In all three environments, the Larmor precession timescale remains shorter than both the k-RAT and the gas drag timescales over most of the investigated grain size range, indicating that B-RAT is the dominant alignment mechanism throughout the spiral galaxy.

The main deviation in the timescales from the original calculations is the separation in magnitude between the arm and interarm k-RAT timescales. In the present reproduction, the difference was found to be approximately two orders of magnitude, whilst LR24 indicate only a difference closer to one order of magnitude. For this reason, the k-RAT timescale only wins over B-RAT for the largest set of grain sizes in the arms, but never does so in the interarms.

In the original work, the median characteristic grain sizes $[a_{\rm align}, a_{\rm disr}]$ were estimated to be $[0.009,\ 0.182]\,\mu$m in the spiral arms, and $[0.019,\ 0.452]\,\mu$m in the interarm region. The angular velocity analysis yielded characteristic grain sizes of $[0.016,\ 0.072]\,\mu$m and $[0.017,\ 0.082]\,\mu$m for Arm 1 and Arm 2, respectively. In the interarm environment, only an alignment threshold was obtained, corresponding to $a_{\rm align} = 0.034\,\mu$m, while no disruption threshold was found within the investigated grain size range.

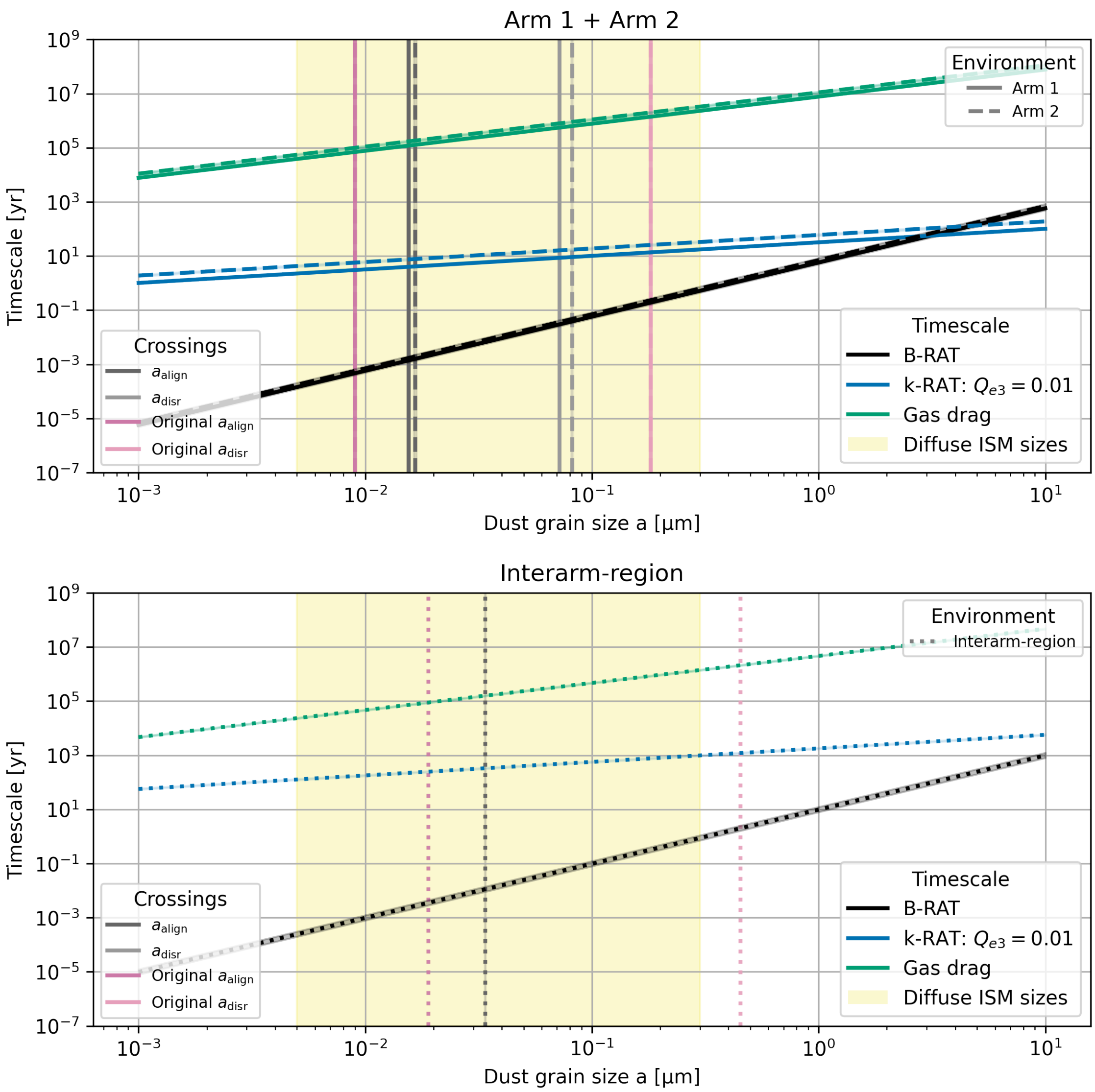

Figure 4.1: Median precession timescales and associated 16th–84th percentile ranges as functions of grain size in the three M51 environments. The upper panel shows the two spiral arm regions and the lower panel shows the interarm region. Vertical grey lines indicate the alignment and disruption grain size thresholds derived from the angular velocity analysis, and the pink indicate the ones from LR24. Input parameters are listed in Table 3.3.

Figure 4.2 shows the same results as in Figure 4.1, but allows k-RAT to depend on the full spectrally averaged radiative torque efficiency $\langle Q(a) \rangle_\lambda$.

With this choice of efficiency, the k-RAT timescale shows a different grain size dependence from the constant Q_{e3} case. At small grain sizes, k-RAT is beaten by the gas drag affecting the grain dynamics, while at larger grain sizes the k-RAT timescale decreases relative to both the gas drag timescale and eventually even beats B-RAT. This behaviour is observed in all three M51 environments.

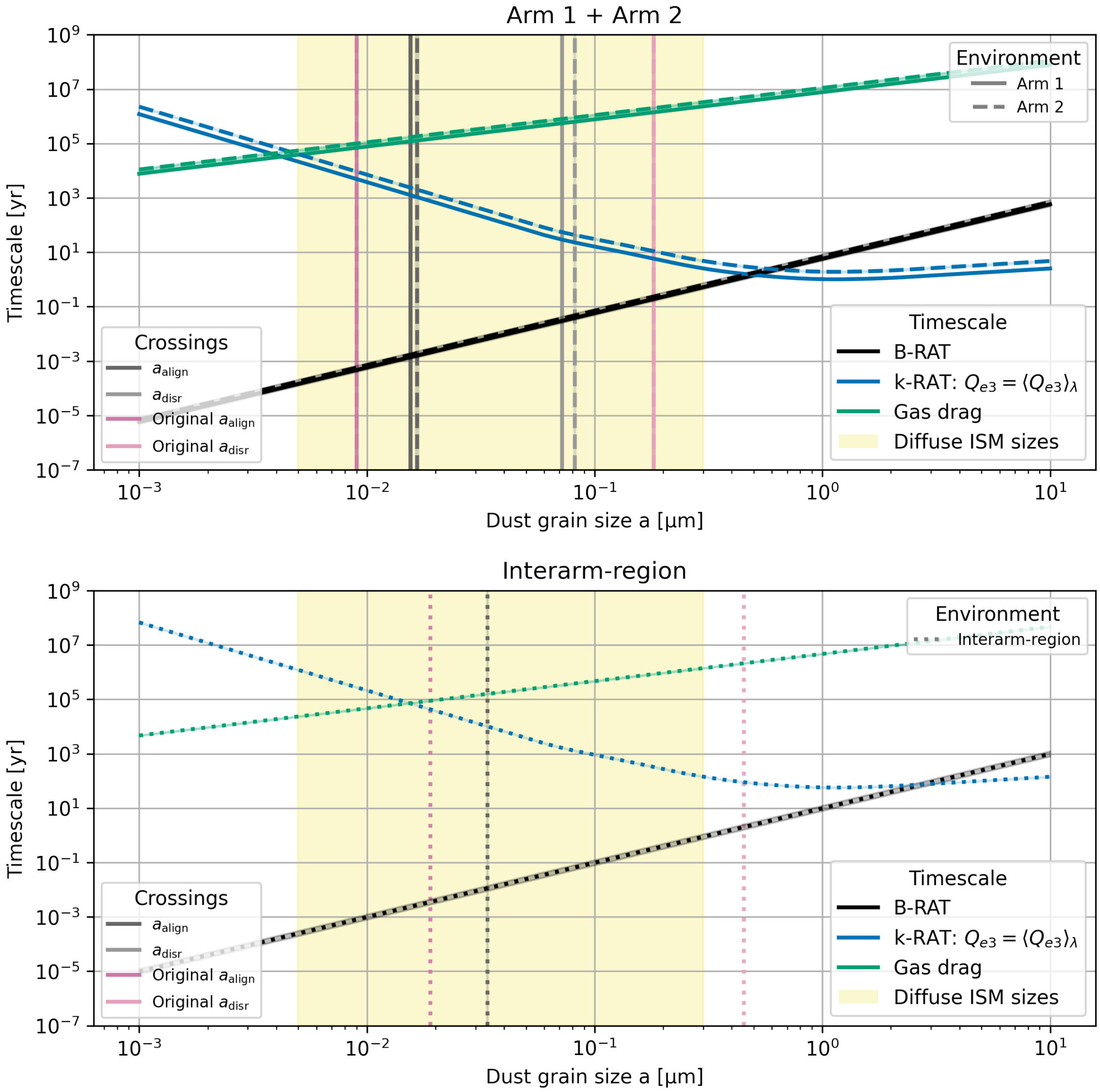

Figure 4.2: Same as Figure 4.1, but k-RAT depends on the wavelength averaged radiative torque efficiency $\langle Q_{e3}(a) \rangle_\lambda$ from Equation 2.19.

The calculated timescales for the IC 10 centre and surrounding regions are shown in Figure 4.3. The input values used are listed in Table 3.4, Section 3.3.2. The results show a greater complexity through the degree of uncertainty in their respective environment, compared to the merely uniformly varied environments of M51.

The behaviour of the k-RAT timescales depends strongly on the adopted radiative torque efficiency. For a constant efficiency of $Q_{e3} = 0.01$, k-RAT can surpass B-RAT only for the largest grains in the central region. When the wavelength averaged efficiency $\langle Q_{e3}(a) \rangle_\lambda$ is used, the k-RAT timescales become shorter than the gas drag timescales at small grain sizes and eventually also becomes shorter than the B-RAT timescale for the larger grain sizes in both environments.

The angular velocity analysis gave characteristic grain sizes of $[0.018,\ 0.128]\,\mu$m in the central region. In the surrounding region, only an alignment threshold is obtained, corresponding to $a_{\text{align}} = 0.041\,\mu$m. No disruption threshold is found within the investigated grain size range. The resulting grain size limits are therefore qualitatively similar to those found for M51.

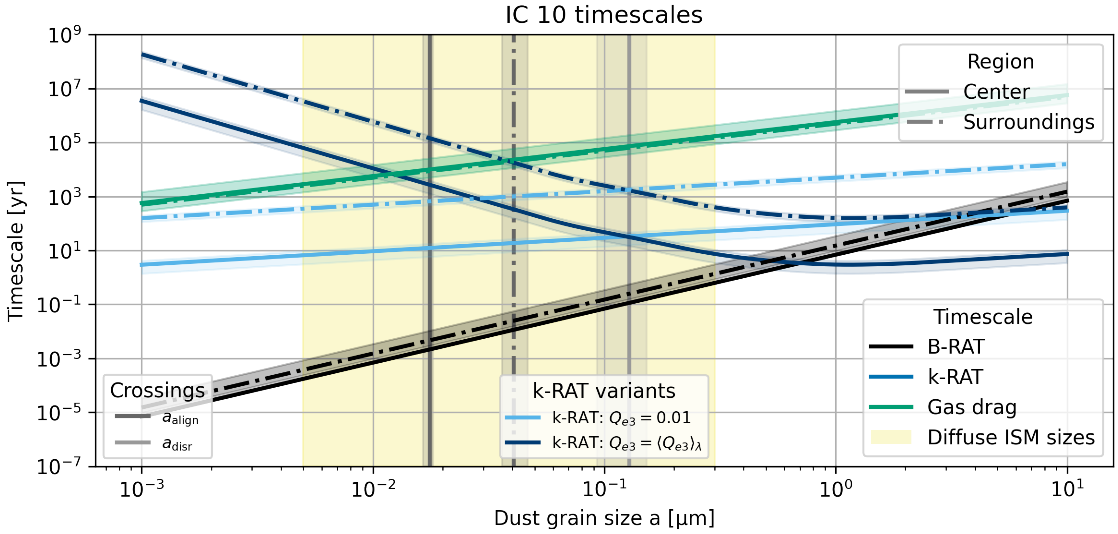

Figure 4.3: Median precession timescales and associated 16th–84th percentile ranges as functions of grain size in the central and surrounding environments of IC 10. Vertical grey lines indicate the characteristic alignment and disruption grain sizes derived from the angular velocity analysis. Input parameters are listed in Table 3.4.

4.3 Alignment and disruption grain sizes

The angular velocity analysis described in Section 3.3 was applied to each environment in M51 and IC 10. Median angular velocities and characteristic grain size thresholds derived from the analysis are shown in Figures 4.4–4.6. For comparison, calculations performed using constant values of $Q_{e3} = 0.01$ and $Q_{e3} = 0.4$ are also displayed.

In the M51 spiral arm environments, both alignment and disruption crossings were obtained for the wavelength averaged radiative torque efficiency. In contrast, the interarm environment only produced an alignment crossing.

For IC 10, both alignment and disruption thresholds were obtained in the central environment, whereas the surrounding environment only produced an alignment threshold. The derived grain size limits are thus qualitatively similar to the ones obtained for the spiral arm and interarm environments of M51 respectively.

It is worth noting that $Q_{e3} = 0.01$ (the light blue line) would not yield any alignment at all in the diffuser regions in the respective galaxies, and only allow alignment of the largest of grain sizes investigated in the denser regions.

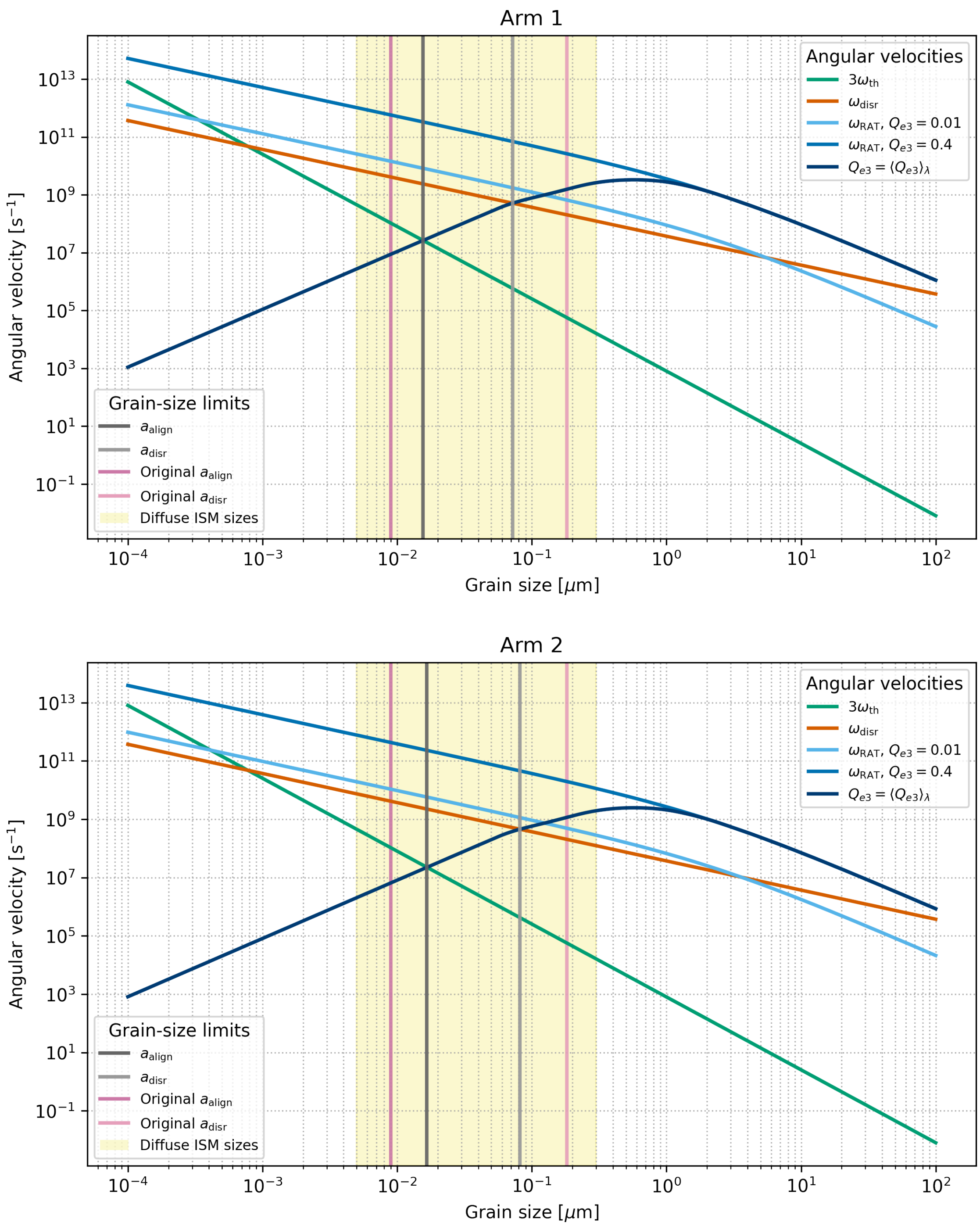

Figure 4.4: Median angular velocities as functions of grain size in the two spiral arm environments of M51. Blue curves show $\omega_{\rm RAT}$ for the three adopted radiative torque efficiency prescriptions, green curves show $3\omega_{\rm th}$, and orange curves show $\omega_{\rm disr}$. Vertical lines indicate alignment and disruption grain size thresholds obtained from the crossing analysis. Pink lines indicate the characteristic grain sizes reported by LR24.

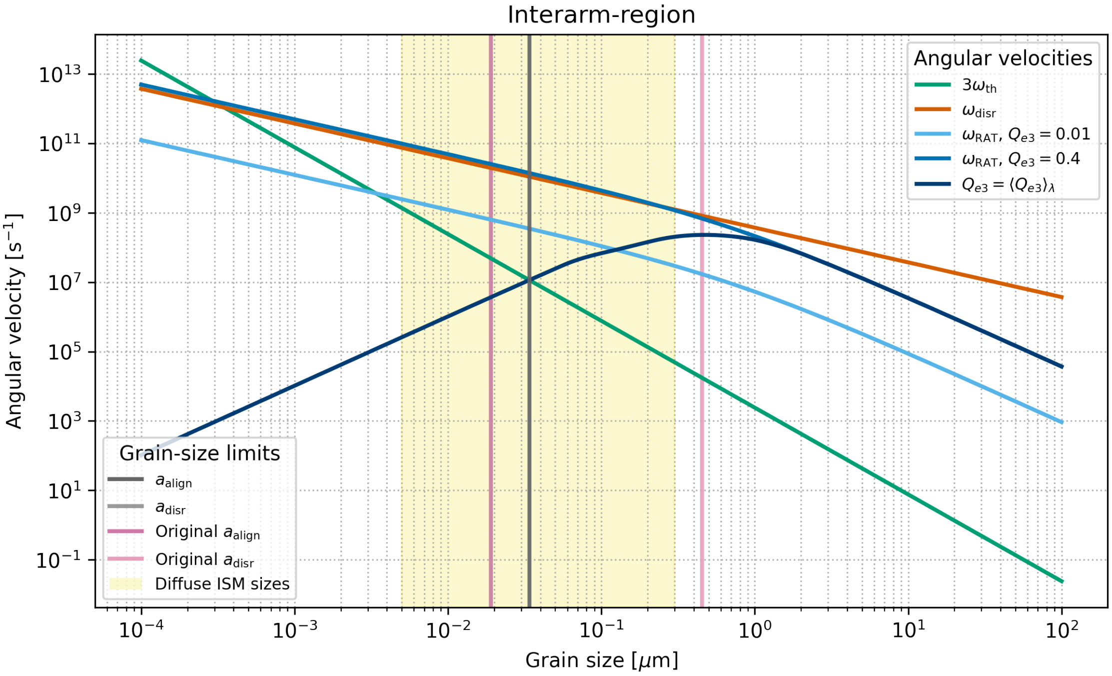

Figure 4.5: Same as Figure 4.4, but for the interarm environment of M51.

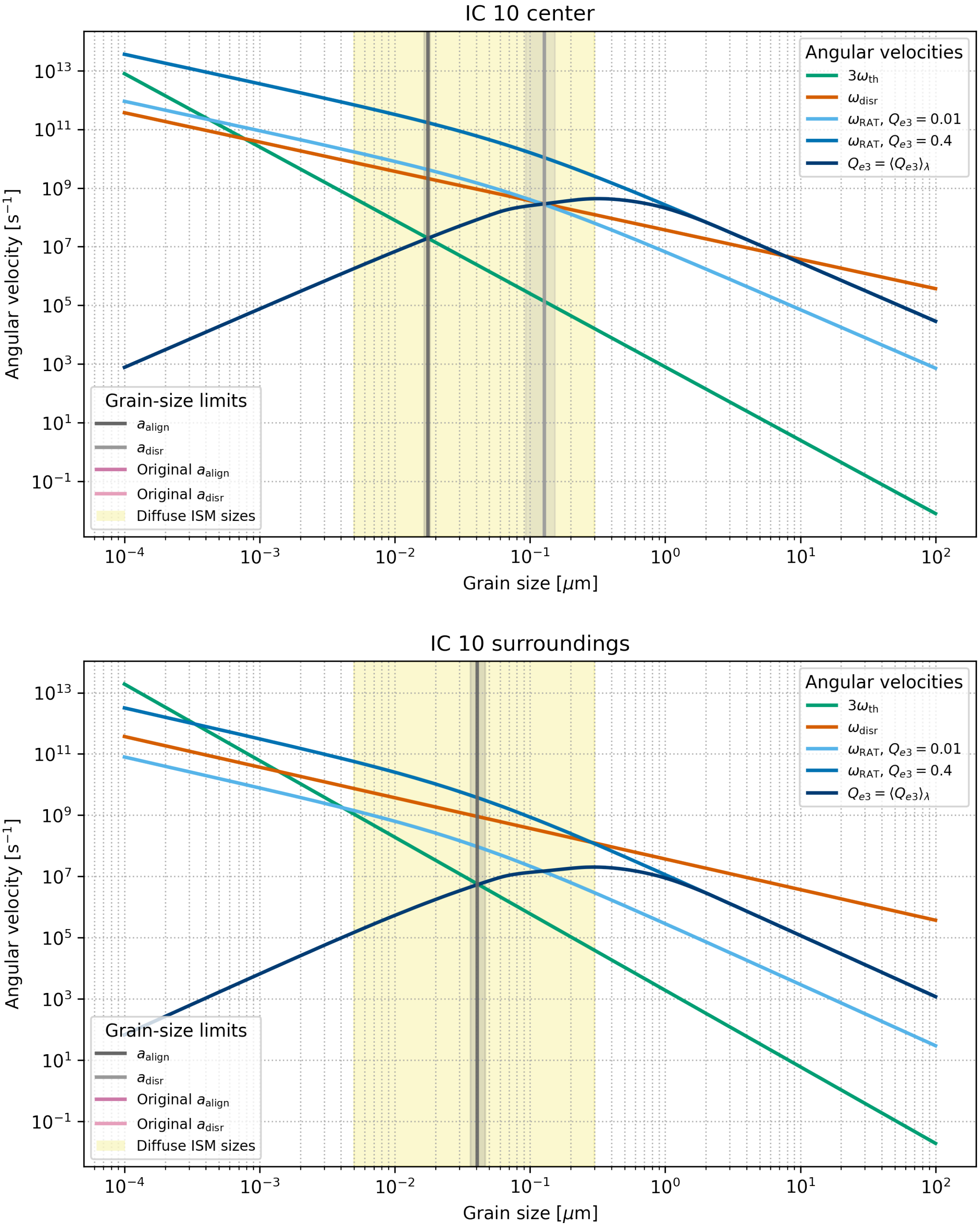

Figure 4.6: Median angular velocities as functions of grain size in the central and surrounding environments of IC 10. Blue curves show $\omega_{\rm RAT}$ for the three adopted radiative torque efficiency prescriptions, green curves show $3\omega_{\rm th}$, and orange curves show $\omega_{\rm disr}$. Vertical lines indicate alignment and disruption grain size thresholds derived from the crossing analysis.

5

Discussion

The discussion is divided into multiple sections. In Section 5.1, the reproduction of M51 is evaluated, after which the results influence by the RAT efficiency factor is discussed in Section 5.2. Section 5.3 talks about the results of the analysis of IC 10 and compares them to the results of M51. From this discussion, speculations on the importance of sensitivity in polarisation measurement are then presented in Section 5.4. Finally, Section 5.5 outlines possible directions for future investigations of polarisation in galaxies and in particular what can be further investigated for IC 10.

5.1 Reproduction of the M51 results

The reproduced M51 calculations recover the overall hierarchy of the timescales as reported by LR24. In all three environments, the Larmor precession timescale remains shorter than both the k-RAT and gas drag timescales over most of the relevant grain size range.

The reproduction does not recover the full spread of the median uncertainty reported by LR24. This is likely a consequence of the simplified environmental maps used in this work, where the input characteristics were represented by uniform distributions or entirely fixed values. Such simplifications cannot fully recreate the real spatial complexity of the spiral arm and interarm environments.

The k-RAT timescales were recreated in the spiral arms by assuming a constant value for the radiative torque efficiency of $Q_{e3} = 10^{-2}$. In the interarm environment however, the reproduced k-RAT timescale became one order of magnitude larger than reported by LR24. Consequently, the reproduction does not catch the transition where k-RAT becomes shorter than B-RAT for the largest grains investigated in the interarm region, as it does in the arms as predicted. This inconsistency is most likely due to the adopted interarm gas temperature and the anisotropy parameter, both of which were estimated from information provided in the LR24 paper, rather than from the exact values used in their calculations.

The numerical crossing analysis returned qualitatively similar grain size limits to those reported by LR24. Both alignment and disruption thresholds were recovered in the spiral arms, while the interarm region only reproduced an alignment size limit. Although the derived grain size thresholds differ quantitatively from those reported by LR24, both approaches (LR24's and the numerical calculation in the present work) lead to the same overall physical picture. The successful reproduction of the timescale hierarchies and the qualitative grain size constraints suggest that the methodology is robust against moderate variations in the adopted environmental parameters.

5.2 Dependence on the radiative torque efficiency

Among all the investigated parameters, the choice of radiative torque efficiency Q_{e3} seems to have one of the strongest effects on the RATs, affecting both the k-RAT timescales and the numerically derived grain size limits via ω_{RAT}. While the choice of a constant value for Q_{e3} had no apparent impact on the overall ordering of the timescales within the physically allowed grain size ranges, it greatly affected the magnitude of the k-RAT timescale. Furthermore, replacing a constant value with the spectrally averaged efficiency $\langle Q_{e3}(a)\rangle_\lambda$ induced a completely different k-RAT behaviour across the entire investigated grain size range. The effect of the choice of Q_{e3} factor is however clearest in the angular velocity analysis.
A constant value was first chosen to replicate the grain size dependence of k-RAT from LR24, and a value of $Q_{e3} = 10^{-2}$, which also was the parameter normalisation value $Q_{e3,-2} = Q_{e2}/10^{-2}$, could most successfully reproduce the published M51 timescales. However, the spectrally averaged efficiency $\langle Q_{e3}(a)\rangle_\lambda$ ended up producing substantially different alignment and disruption limits in both galaxies when applied to the numerical crossing method. The spectrally averaged efficiency produced alignment and disruption thresholds in the denser environments of both galaxies while suppressing disruption in the two more diffuse environments. This behaviour in ω_{RAT} and the consequent grain size thresholds could not be reproduced with either of the investigated constant values for the torque efficiency.
The calculation of $\langle Q_{e3}(a)\rangle_\lambda$ was based on the spectral energy distribution of the local Milky Way radiation field. A different radiation spectrum could therefore effect both the magnitude and grain size dependence of the RAT efficiency on a whole. Furthermore, these results suggest that the choice of RAT efficiency itself may be a significant source of uncertainty in RAT-based grain alignment studies such as LR24.
The comparison performed in this work demonstrates that different assumptions of Q_{e3} can lead to significantly different alignment and disruption thresholds. Future investigations would therefore benefit both from calculating spectrally averaged efficiencies using galaxy specific radiation fields, and from investigating the sensitivity of the results to the choice of the RAT efficiency.

5.3 Application to IC 10

Having concluded that the adopted methodology, extended with the angular velocity calculations, qualitatively reproduces the results of LR24, the same procedure was applied to IC 10. Despite the differences between the two galaxies ISM environments, the resulting timescale hierarchies and grain size limit exhibit notable similarities. The IC 10 centre greatly resembles the M51 spiral arm environments, while the IC 10 surroundings resemble the M51 interarm region. With room for some amount of quantitative variation, these paralells are reflected in both the timescale calculations

and the angular velocity analysis.
The alignment thresholds calculated for the IC 10 centre are comparable to those obtained for the spiral arms of M51, whereas the surrounding region returned an alignment limit similar to the one for the M51 interarm environment. Likewise, disruption thresholds were recovered only in the denser environments of both galaxies, while the respective more diffuse regions didn't produce disruption crossings within the investigated grain size range.
These parallels can be traced to the adopted environmental parameters. As shown in Tables 3.3 and 3.4, the magnetic field strengths and dust temperatures adopted for the IC 10 centre are comparable to those used for the M51 spiral arm environments. Likewise, the IC 10 surroundings share several characteristics with the M51 interarm region, including weaker magnetic fields and lower radiation energy densities. The main deviations in the timescale and grain size threshold results stem mostly from the influence of their substantial differences in gas column densities, volume densities and the magnitude of the energy densities from the respective radiation fields. The energy density in the centre region is of almost the same magnitude as in the interarms of M51 while the surrounding has a much weaker energy density of only about a third the strength of the centre.
The angular velocity analysis suggests that the radiation field will have a biggest say in whether grain disruption will occur. In both M51 and IC 10, the denser environments produce RAT angular velocities that systematically come to surpass both the thermal and disruption velocity limits over part of the investigated grain size range, which result in both alignment and disruption thresholds. In contrast, the diffuse environments have weaker radiation energy densities, so the RAT angular velocities never increase enough in the range of longer grain sizes to reach the critical disruption velocity. Therefore no disruption thresholds were obtained within the investigated grain size range for the M51 interarm region nor the IC 10 surroundings. This suggests that weaker radiation fields may suppress rotational disruption by limiting the rotational acceleration of the larger grains.

5.4 Predicitons of grain alignment and FIR polarisation

The alignment and numerical crossing analysis indicate that dust grain alignment should be possible throughout both the investigated regions of IC 10. Alignment thresholds were obtained in both the central and surrounding region, and the resulting grain size constraints are comparable to those obtained in M51.
This appears inconsistent with the conclusions that were drawn in the LR24 paper based on their results of M51. There they interpreted the observed variations in polarisation efficiency between the environments by the change in the disruption limit caused by RAT-D. In their analysis of M51, the spiral arm environments produce shorter disruption thresholds than in the interarm region, meaning that grains can't become as large in the arms as they can in the interarms before they are disrupted into smaller grains. Because large dust grains are more efficient in emitting polarised FIR radiation (see Figure 3 of Hensley & Draine [19]), their fragmentation in the

arms directly reduces the arms polarisation efficiency, compared to the interarms where larger grains remain.
If grain alignment is present throughout IC 10, polarised emission would be expected to be detected not only in the central region, but at some noteworthy efficiency in the surroundings as well. However, from the survey by SOFIA/HAWC+, significant polarised FIR emission is detected only in the central region of IC 10. This apparent inconsistency may indicate that the absence of a polarisation detection in the surroundings is observational rather than physical.
The central region is much brighter than the surroundings, and exhibits energy densities comparable to those of the M51 interarms - where polarisation is detected to some great efficiency. Consequently, the absence of polarisation detected outside the centre region may rather reflect inadequate sensitivity of the observations rather than a lack of aligned grains. Under this hypothesis, grain alignment remains possible throughout both the investigated regions of IC 10, while only the brightest regions, those in the vicinity of an active starburst, produce detectable polarised FIR emission.
This is consistent with observations of other SOFIA/HAWC+ targets. For example observations of 30 Doradus with SOFIA by Tram et al. [10] which reveal widespread polarised emission around the centre of the nebula. Those regions where observed with total intensities (Stokes I) up to 30 Jy/arcsec^2 (Figure 2 of Tram et al. 2021 [10]). In contrast, the IC 10 observation with SOFIA shown in Figure 3.2 exhibit total intensities of only 0.001–0.007 Jy/arcsec^2. The much lower surface brightness of the IC 10 to those where polarisation could be detected in 30 Doradus may therefore explain why grain alignment can still be present in the surroundings while not producing a sufficient polarisation signal to have been detected by SOFIA.

5.5 Caveats and future work

The modified blackbody fitting may be a source of uncertainty carried over from the Herschel data into the RAT analysis. In particular, the dust temperature map was used to estimate the local radiation field energy density in IC 10, and therefore affect the derived k-RAT timescales, RAT angular velocities, and disruption thresholds. The PACS bands were intentionally excluded to avoid the clear calibration inconsistencies with Planck, but this also means that the final dust temperature estimate relies only on the spectral energy distribution of the SPIRE bands, which visibly showed to contain foreground contamination from the Milky Way. Therefore, from comparing the Herschel derived gas column density to the VLA H I indicates that the dust-based N_H is strongly affected by the foreground contamination. For this reason, the VLA H I map was adopted in place for the gas column density, keeping only the derived dust temperature in the RAT analysis. But because the dust temperature and gas column density weren't produced independently, the apparent effect of the contamination in the N_H map likely has more subtle effects on the T_d map. If further progression of the Herschel MBB fitting process should be investigated, one is encouraged to adopt a double MBB fit in order to remove the contamination from the Milky Way foreground in the Herschel SPIRE maps. One should then also derive the appropriate double MBB colour corrections for the

SPIRE bands, using the code and methodology from the SPIRE Handbook [32].
The comparison performed in this work indicates that the radiation field plays a central role in determining both the k-RAT timescales and the resulting grain size constraints, due to its influence on the radiative torque. Future investigations of RATs would therefore benefit from using observationally derived radiation field maps where possible. Computing the spectrally averaged torque as a whole with such maps would also allow for a more direct assessment of the environmental dependence of grain alignment and on RAT-D.
The variations of the environmental properties were chosen often from random/uniform distributions (e.g. for the magnetic field strength). A future analysis would benefit from more realistic environmental variations, e.g. by using maps of the magnetic field strength, volume density, gas temperature etc, which would then ensure proper spatial coupling between these various properties.

6

Conclusions

In this work, dust grain alignment was investigated in the dwarf galaxy IC 10 using the framework adopted by Lopez-Rodriguez & Tram (2024) [27] for M51. Before applying the methodology to IC 10, the published results on M51 were first successfully reproduced. Even though the exact precession timescales and grain size thresholds exhibit quantitative differences, the reproduction could recover the same overall environmental characteristics and the qualitative hierarchy of their timescales. This indicates that the methodology adopted and further developed in this work is adequately robust to be applied to galactic environments beyond the spiral galaxy M51.

The application of the methodology onto IC 10 implied that dust grain alignment with the magnetic field is possible throughout the galaxy. It could therefore be successfully demonstrated that dust grain alignment remains possible in ISM conditions that substantially differ from those of a Milky Way-like galaxy. Alignment thresholds were recovered for both the central star forming region and the diffuser region surrounding the centre of IC 10, and the resulting constraints on the grain sizes were comparable to the ones found in M51.

The analysis further suggests that the strength of the environment's radiation field plays a key role as to whether grain disruption will occur. In both M51 and IC 10, disruption thresholds were obtained only in the denser environments (the spiral arms and star forming centre respectively), while the more diffuse regions produced grain size limits for alignment but no "upper limit" for disruption.

Herschel observations were modelled with modified black body SED fitting to derive the dust temperature throughout the galaxy with some limitations to the methods from the data. Namely, the Herschel PACS maps had an unknown zero-point offset which could not be easily recovered by comparing to Planck data, and the SPIRE maps were partially contaminated with foreground emission. In the end only the SPIRE data was used but because of the contamination in the gas column density this could not be applied in the final analysis. If further progression of this Herschel MBB fitting process should be investigated, one is encouraged to adopt a fit of a double MBB with accompanying colour corrections, to remove the contamination in the Herschel SPIRE maps from the Milky Way foreground.

Finally, the predictions from the RAT study together with the SOFIA/HAWC+ observations of IC 10 indicate that the RAT analysis can indeed establish the possibility of grain alignment, but may not by itself be sufficient to determine if polarisation will be observed. Although the calculations suggest that aligned grains may exist throughout IC 10, significant polarised FIR emission is detected only where the radiation is sufficient to be detected, near the star bursting regions. This suggests that

observational sensitivity may be an important factor when interpreting polarisation observations of faint systems in the Universe, and that the absence of a polarisation detection may not necessarily imply the absence of aligned dust grains.
The calculations for the minimum size of aligned grains showed substantial differences between the center and the surroundings of IC 10. This would predict differences in the wavelength dependence of optical polarisation between the two regions (with a peak at shorter wavelengths in the center versus the surroundings). It would be interesting to follow up this work with multi-band observations of diffuse optical light in IC 10 to investigate whether this prediction is borne out.

Bibliography

[1] D. C. B. Whittet. *Dust in the Galactic Environment*. Institute of Physics, 2003.

[2] S. Bianchi. Revisiting the local interstellar radiation field using <i>gaia</i> dr3. *Astronomy amp; Astrophysics*, 691:A330, November 2024.

[3] Thiem Hoang, Le Ngoc Tram, Hyeseung Lee, Pham Ngoc Diep, and Nguyen Bich Ngoc. Grain alignment and disruption by radiative torques in dense molecular clouds and implication for polarization holes. *The Astrophysical Journal*, 908(2):218, 2021.

[4] Alejandro S. Borlaff, Enrique Lopez-Rodriguez, Rainer Beck, Rodion Stepanov, Eva Ntormousi, Annie Hughes, Konstantinos Tassis, Pamela M. Marcum, Lucas Grosset, and John E. Beckman. Extragalactic magnetism with sofia (legacy program). i. the magnetic field in the multiphase interstellar medium of m51. *The Astrophysical Journal*, 921(2):128, 2021.

[5] Alejandro S. Borlaff, Enrique Lopez-Rodriguez, Rainer Beck, Susan E. Clark, Evangelia Ntormousi, Konstantinos Tassis, Sergio Martin-Alvarez, Mehrnoosh Tahani, Daniel A. Dale, Ignacio del Moral-Castro, Julia Roman-Duval, Pamela M. Marcum, John E. Beckman, Kandaswamy Subramanian, Sarah Eftekharzadeh, and Leslie Proudfit. Extragalactic magnetism with sofia (salsa legacy program). v. first results on the magnetic field orientation of galaxies. *The Astrophysical Journal*, 952(1):4, 2023.

[6] John S. Hall and Alfred H. Mikesell. Observations of polarized light from stars. , 54:187–188, September 1949.

[7] W. A. Hiltner. On the Presence of Polarization in the Continuous Radiation of Stars. II. , 109:471, May 1949.

[8] B.-G. Andersson, A. Lazarian, and J. Vaillancourt. Interstellar dust grain alignment. *Annual Review of Astronomy and Astrophysics*, 53:501–539, 2015.

[9] Ryo Tazaki, Hidekazu Tanaka, Satoshi Okuzumi, Akimasa Kataoka, and Hideko Nomura. Light scattering by porous dust aggregates. i. angular dependence. *The Astrophysical Journal*, 839(1):56, 2017.

[10] Le Ngoc Tram, Thiem Hoang, Enrique Lopez-Rodriguez, Simon Coudé, Archana Soam, B-G Andersson, Min-Young Lee, Lars Bonne, William D. Vacca, and Hyeseung Lee. Sofia observations of 30 doradus. i. far-infrared dust polarization and implications for grain alignment and disruption by radiative torques. *The Astrophysical Journal*, 923(1):130, December 2021.

[11] B. Namumba, Claude Carignan, Tim Foster, and N. Deg. H i observations of ic 10 with the drao synthesis telescope. *Monthly Notices of the Royal Astronomical Society*, 490(3):3365–3377, 2019.

[12] Ioana A. Stelea, Snezana Stanimirovic, Nickolas M. Pingel, Hongxing Chen, Eric W. Koch, Adam K. Leroy, Erik Rosolowsky, Chang-Goo Kim, Alberto D. Bolatto, Julianne J. Dalcanton, Michael P. Busch, Harrisen Corbould, J. R. Dawson, Cosima Eibensteiner, Amanda Kepley, Melanie Krips, Claire E. Murray, Julia Roman-Duval, Daniel R. Rybarczyk, Evan D. Skillman, Elizabeth Tarantino, Vicente Villanueva, and Thomas G. Williams. The local group l-band survey: Probing cold atomic gas in ic10 with neutral hydrogen absorption, 2025.

[13] NASA/IPAC Extragalactic Database. Results for ic 10. `https://ned.ipac.caltech.edu/byname?objname=IC+10`, 2026. Operated by the California Institute of Technology under contract with NASA. Accessed 18 April 2026.

[14] Sidney Van den Bergh. *Galaxies of the Local Group*. Cambridge University Press, Cambridge, 2000.

[15] Adam Leroy, Alberto Bolatto, Fabian Walter, and Leo Blitz. Molecular gas in the low-metallicity, star-forming dwarf ic 10. *The Astrophysical Journal*, 643(2):825–843, 2006.

[16] F. Annibali, A. M. N. Ferguson, P. M. Sanchez-Alarcon, P. Dimauro, L. K. Hunt, R. Pascale, M. Bellazzini, A. Lançon, P. Jablonka, J. M. Howell, K. Voggel, J. C. Cuillandre, Abdurro'uf, G. Battaglia, L. R. Bedin, Michele Cantiello, D. Carollo, P. A. Duc, S. S. Larsen, M. Libralato, F. R. Marleau, D. Massari, T. Saifollahi, C. Tortora, M. Urbano, M. Gatto, I. McDonald, M. Baes, J. Román, E. Dalessandro, E. Iodice, R. Ragusa, S. Pearson, S. Andreon, N. Auricchio, C. Baccigalupi, M. Baldi, A. Balestra, S. Bardelli, P. Battaglia, A. Biviano, E. Branchini, M. Brescia, S. Camera, G. Cañas-Herrera, V. Capobianco, C. Carbone, J. Carretero, S. Casas, M. Castellano, G. Castignani, S. Cavuoti, A. Cimatti, C. Colodro-Conde, G. Congedo, C. J. Conselice, L. Conversi, Y. Copin, F. Courbin, H. M. Courtois, M. Cropper, H. Degaudenzi, G. De Lucia, H. Dole, F. Dubath, C. A. J. Duncan, X. Dupac, S. Escoffier, M. Farina, R. Farinelli, S. Ferriol, F. Finelli, M. Frailis, E. Franceschi, M. Fumana, S. Galeotta, K. George, B. Gillis, C. Giocoli, J. Gracia-Carpio, A. Grazian, F. Grupp, S. V. H. Haugan, H. Hoekstra, W. Holmes, I. M. Hook, F. Hormuth, A. Hornstrup, K. Jahnke, M. Jhabvala, E. Keihänen, S. Kermiche, A. Kiessling, B. Kubik, M. Kümmel, M. Kunz, H. Kurki-Suonio, R. Laureijs, A. M. C. Le Brun, S. Ligori, P. B. Lilje, V. Lindholm, I. Lloro, G. Mainetti, D. Maino, E. Maiorano, O. Mansutti, S. Marcin, O. Marggraf, M. Martinelli, N. Martinet, F. Marulli, R. J. Massey, E. Medinaceli, S. Mei, M. Melchior, Y. Mellier, M. Meneghetti, E. Merlin, G. Meylan, A. Mora, M. Moresco, L. Moscardini, R. Nakajima, C. Neissner, S. M. Niemi, C. Padilla, S. Paltani, F. Pasian, K. Pedersen, W. J. Percival, V. Pettorino, S. Pires, G. Polenta, M. Poncet, L. A. Popa, L. Pozzetti, F. Raison, R. Rebolo, A. Renzi, J. Rhodes, G. Riccio, E. Romelli, M. Roncarelli, R. Saglia, Z. Sakr, D. Sapone, B. Sartoris, M. Schirmer, P. Schneider, A. Secroun, G. Seidel, S. Serrano, P. Simon, C. Sirignano, G. Sirri, L. Stanco, J. Steinwagner, P. Tallada-Crespí, A. N. Taylor, I. Tereno, N. Tessore, S. Toft, R. Toledo-Moreo, F. Torradeflot, I. Tutusaus, L. Valenziano, J. Valiviita, T. Vassallo, A. Veropalumbo, Y. Wang, J. Weller, G. Zamorani, I. A. Zinchenko, E. Zucca, J. García-Bellido, J. Martín-Fleitas,

and V. Scottez. Euclid: Early release observations – the extended stellar component of the ic10 dwarf galaxy, 2026.

[17] Aritra Basu, Sambit Roychowdhury, Volker Heesen, Rainer Beck, Elias Brinks, Jonathan Westcott, and Luke Hindson. New insights into the interstellar medium of the dwarf galaxy ic 10: connection between magnetic fields, the radio–infrared correlation and star formation. *Monthly Notices of the Royal Astronomical Society*, 471(1):337–354, 2017.

[18] Bruce T. Draine. *Physics of the Interstellar and Intergalactic Medium.* Princeton University Press, Princeton, NJ, 2011.

[19] Brandon S. Hensley and Bruce T. Draine. The astrodust+pah model: A unified description of the extinction, emission, and polarization from dust in the diffuse interstellar medium. *The Astrophysical Journal*, 2023.

[20] B. T. Draine and Brandon S. Hensley. Using the starlight polarization efficiency integral to constrain shapes and porosities of interstellar grains. *The Astrophysical Journal*, 919(1):65, 2021.

[21] J. S. Mathis, W. Rumpl, and K. H. Nordsieck. The size distribution of interstellar grains. , 217:425–433, October 1977.

[22] B. T. Draine and Joseph C. Weingartner. Radiative torques on interstellar grains. i. superthermal spin-up. *The Astrophysical Journal*, 470:551, October 1996.

[23] B.T. Draine. Interstellar dust grains. *Annual Review of Astronomy and Astrophysics*, 41(1):241–289, 2003.

[24] Allan H. Morrish. *The Physical Principles of Magnetism.* Robert E. Krieger Publishing Company, Huntington, NY, 1980.

[25] B. T. Draine. Optical and magnetic properties of dust grains, 1996.

[26] A. Lazarian and Thiem Hoang. Radiative torques: analytical model and basic properties. *Monthly Notices of the Royal Astronomical Society*, 378(3):910–946, 2007.

[27] Enrique Lopez-Rodriguez and Le Ngoc Tram. Probing the dust grain alignment mechanisms in spiral galaxies with m51 as the case study. *The Astrophysical Journal*, 975(1):119, 2024.

[28] W. G. Roberge, T. A. Degraff, and J. E. Flaherty. Magnetic relaxation and alignment of interstellar grains. *The Astrophysical Journal*, 418:287–301, 1993.

[29] Thiem Hoang. Rotational disruption of astrophysical dust and ice—theory and applications. *Galaxies*, 8(3):52, 2020.

[30] Enrique Lopez-Rodriguez, Sui Ann Mao, Rainer Beck, Alejandro S. Borlaff, Evangelia Ntormousi, Konstantinos Tassis, Daniel A. Dale, Julia Roman-Duval, Kandaswamy Subramanian, Sergio Martin-Alvarez, Pamela M. Marcum, Susan E. Clark, William T. Reach, Doyal A. Harper, and Ellen G. Zweibel. Extragalactic magnetism with sofia (salsa legacy program). iv. program overview and first results on the polarization fraction*. *The Astrophysical Journal*, 936(1):92, 2022.

[31] ESA Herschel Science Centre. *PACS Products Explained.* Technical documentation, Accessed 2026-06-01.

[32] ESA Herschel Science Centre. *SPIRE Handbook.* Accessed 2026-06-01.

[33] Astropy Collaboration, Adrian M. Price-Whelan, Pey Lian Lim, et al. The Astropy Project: Sustaining and Growing a Community-oriented Open-source Project and the Latest Major Release (v5.0) of the Core Package. *The Astrophysical Journal*, 935(2):167, 2022.

[34] G. Aniano, B. T. Draine, K. D. Gordon, and K. Sandstrom. Common-Resolution Convolution Kernels for Space- and Ground-Based Telescopes. , 123(908):1218, October 2011.

[35] Thomas Robitaille, Christoph Deil, Adam Ginsburg, et al. reproject: Astronomical image reprojection in python.

[36] Yancy L. Shirley, Jeffrey G. Mangum, Desika Narayanan, and James Di Francesco. How to use thermal dust continuum emission to measure the physical properties of dusty astrophysical objects. *Publications of the Astronomical Society of the Pacific*, 138:043001, 2026.

[37] Kristen Gillmon, J. Michael Shull, Jason Tumlinson, and Charles Danforth. A<i>fuse</i>survey of interstellar molecular hydrogen toward high-latitude agns. *The Astrophysical Journal*, 636(2):891–907, January 2006.

[38] Ava Polzin, Andrey V. Kravtsov, Vadim A. Semenov, and Nickolay Y. Gnedin. Modeling molecular hydrogen in low-metallicity galaxies. *The Astrophysical Journal*, 966(2):172, may 2024.

[39] Matthew Newville, Renee Otten, Andrew Nelson, et al. Lmfit: Non-linear least-squares minimization and curve-fitting for python, 2025.

[40] Polles, F. L., Madden, S. C., Lebouteiller, V., Cormier, D., Abel, N., Galliano, F., Hony, S., Karczewski, O. L., Lee, M.-Y., Chevance, M., Galametz, M., and Lianou, S. Modeling ionized gas in low-metallicity environments: the local group dwarf galaxy ic 10. *A&A*, 622:A119, 2019.

[41] Alberto D. Bolatto, James M. Jackson, Christine D. Wilson, and Gerald Moriarty-Schieven. Submillimeter observations of ic 10: The dust properties and neutral carbon content of a low-metallicity starburst. *The Astrophysical Journal*, 532(2):909–921, 2000.

[42] ESA Herschel Science Centre. *PACS Explanatory Supplement.* Accessed 2026-06-01.

[43] ESA Herschel Science Centre. *PACS Photometer Passbands and Colour Correction Factors for Various Source SEDs.* Technical note, Accessed 2026-06-01.

[44] Planck Collaboration, Aghanim, N., Ashdown, M., Aumont, J., Baccigalupi, C., Ballardini, M., Banday, A. J., Barreiro, R. B., Bartolo, N., Basak, S., Benabed, K., Bernard, J.-P., Bersanelli, M., Bielewicz, P., Bonavera, L., Bond, J. R., Borrill, J., Bouchet, F. R., Boulanger, F., Burigana, C., Calabrese, E., Cardoso, J.-F., Carron, J., Chiang, H. C., Colombo, L. P. L., Comis, B., Couchot, F., Coulais, A., Crill, B. P., Curto, A., Cuttaia, F., de Bernardis, P., de Zotti, G., Delabrouille, J., Di Valentino, E., Dickinson, C., Diego, J. M., Doré, O., Douspis, M., Ducout, A., Dupac, X., Dusini, S., Elsner, F., Enßlin, T. A., Eriksen, H. K., Falgarone, E., Fantaye, Y., Finelli, F., Forastieri, F., Frailis, M., Fraisse, A. A., Franceschi, E., Frolov, A., Galeotta, S., Galli, S., Ganga, K., Génova-Santos, R. T., Gerbino, M., Ghosh, T., Giraud-Héraud, Y., González-Nuevo, J., Górski, K. M., Gruppuso, A., Gudmundsson, J. E., Hansen, F. K., Helou, G., Henrot-Versillé, S., Herranz, D., Hivon, E., Huang, Z., Jaffe, A. H., Jones,

W. C., Keihänen, E., Keskitalo, R., Kiiveri, K., Kisner, T. S., Krachmalnicoff, N., Kunz, M., Kurki-Suonio, H., Lamarre, J.-M., Langer, M., Lasenby, A., Lattanzi, M., Lawrence, C. R., Le Jeune, M., Levrier, F., Lilje, P. B., Lilley, M., Lindholm, V., López-Caniego, M., Ma, Y.-Z., Macías-Pérez, J. F., Maggio, G., Maino, D., Mandolesi, N., Mangilli, A., Maris, M., Martin, P. G., Martínez-González, E., Matarrese, S., Mauri, N., McEwen, J. D., Melchiorri, A., Mennella, A., Migliaccio, M., Miville-Deschênes, M.-A., Molinari, D., Moneti, A., Montier, L., Morgante, G., Moss, A., Natoli, P., Oxborrow, C. A., Pagano, L., Paoletti, D., Patanchon, G., Perdereau, O., Perotto, L., Pettorino, V., Piacentini, F., Plaszczynski, S., Polastri, L., Polenta, G., Puget, J.-L., Rachen, J. P., Racine, B., Reinecke, M., Remazeilles, M., Renzi, A., Rocha, G., Rosset, C., Rossetti, M., Roudier, G., Rubiño-Martín, J. A., Ruiz-Granados, B., Salvati, L., Sandri, M., Savelainen, M., Scott, D., Sirignano, C., Sirri, G., Soler, J. D., Spencer, L. D., Suur-Uski, A.-S., Tauber, J. A., Tavagnacco, D., Tenti, M., Toffolatti, L., Tomasi, M., Tristram, M., Trombetti, T., Valiviita, J., Van Tent, F., Vielva, P., Villa, F., Vittorio, N., Wandelt, B. D., Wehus, I. K., Zacchei, A., and Zonca, A. Planck intermediate results - xlviii. disentangling galactic dust emission and cosmic infrared background anisotropies. *A&A*, 596:A109, 2016.

[45] Lombardi, Marco, Bouy, Hervé, Alves, João, and Lada, Charles J. Herschel-planck dust optical-depth and column-density maps - i. method description and results for orion. *A&A*, 566:A45, 2014.

[46] Eric W. Koch, Adam K. Leroy, Erik W. Rosolowsky, Laura Chomiuk, Julianne J. Dalcanton, Nickolas M. Pingel, Sumit K. Sarbadhicary, Snežana Stanimirović, Fabian Walter, Haylee N. Archer, Alberto D. Bolatto, Michael P. Busch, Hongxing Chen, Ryan Chown, Harrisen Corbould, Serena A. Cronin, Jeremy Darling, Thomas Do, Jennifer Donovan Meyer, Cosima Eibensteiner, Deidre Hunter, Rémy Indebetouw, Preshanth Jagannathan, Amanda A. Kepley, Chang-Goo Kim, Shin-Jeong Kim, Timea O. Kovacs, Joshua Marvil, Eric J. Murphy, Claire E. Murray, Jürgen Ott, D.J. Pisano, Mary Putman, Daniel R. Rybarczyk, Julia Roman-Duval, Karin Sandstrom, Eva Schinnerer, Evan D. Skillman, Adam Smercina, Ioana Stelea, Jay Strader, Jiayi Sun, Devisree Tallapaneni, Elizabeth Tarantino, Vicente Villanueva, Daniel R. Weisz, Thomas G. Williams, and Tony Wong. The karl g. jansky very large array local group <i>l</i>-band survey (lglbs). *The Astrophysical Journal Supplement Series*, 279(2):35, 2025.

[47] K. T. Chyży, J. Knapik, D. J. Bomans, U. Klein, R. Beck, M. Soida, and M. Urbanik. Magnetic fields and ionized gas in the local group irregular galaxies ic 10 and ngc 6822. *Astronomy & Astrophysics*, 405:513–524, 2003.

7

Appendix 1

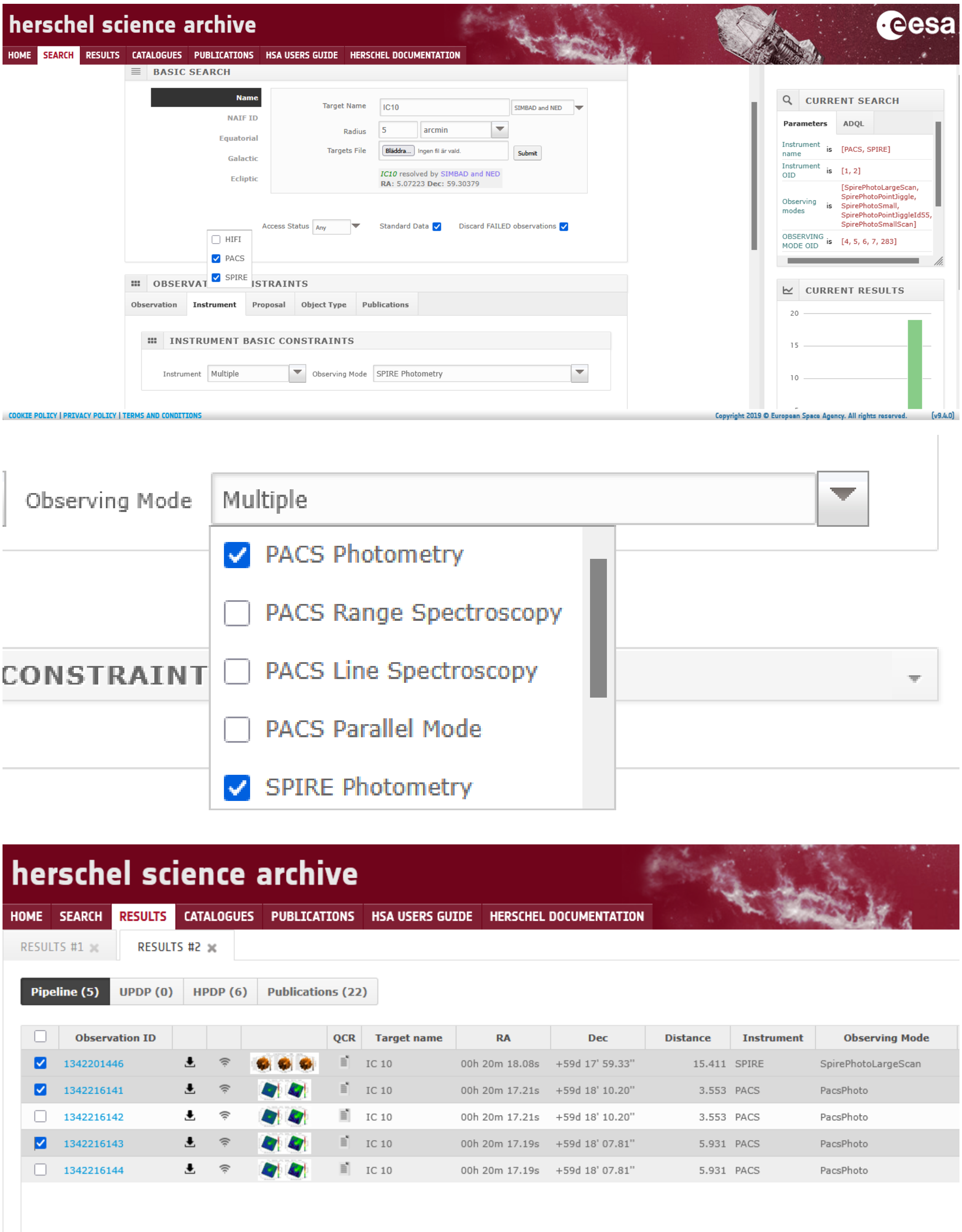

Figure 7.1: Results from search in the Herschel Science Archive.

DEPARTMENT OF SPACE, EARTH AND ENVIRONMENT
CHALMERS UNIVERSITY OF TECHNOLOGY
Gothenburg, Sweden
www.chalmers.se

CHALMERS
UNIVERSITY OF TECHNOLOGY